

Seasonal Variation of Polar Ice: Implications for Ultrahigh Energy Neutrino Detectors

A. Kyriacou,* S. Prohira, and D. Besson

Department of Physics and Astronomy, University of Kansas
Lawrence, KS, USA

The upper 100 m to 150 m of the polar ice sheet, called the firn, has a time-dependent density due to seasonal variations in the surface temperature and snow accumulation. We present RF simulations of an in-ice neutrino-induced radio source that show that these density anomalies create variations in the amplitude and propagation times of radio signals propagating through polar firn at an altitude of ~ 3000 m above sea level. The received power from signals generated in the ice that refract within the upper ~ 15 m firn are subject to a seasonal variation on the order of 10%. These variations result in an irreducible background uncertainty on the reconstructed neutrino energy and arrival direction for detectors using ice as a detection medium.

I. INTRODUCTION

For decades the ultrahigh energy neutrino (UHEN) flux, with energies exceeding 10 PeV, has been predicted to exist as a by-product of ultrahigh energy cosmic rays (UHECRs) interacting with ambient photons [1, 2]. The UHEN flux is likely composed of two populations associated with distinct production mechanisms. At lower energies, an *astrophysical* flux arises from cosmic ray-photon interactions within the sources themselves, such as active galactic nuclei (AGNs), supernova remnants, and other compact objects [3]. At higher energies, cosmic rays escape their sources and propagate through intergalactic space, where they scatter off relic photons of the cosmic microwave background (CMB). For UHECR protons with energies above the ‘Greisen-Zatsepin-Kuzmin’ (GZK) limit of $E > 5 \cdot 10^{19}$ eV, this interaction produces neutral and charged pions that subsequently decay into photons and neutrinos respectively, the latter of which comprise the *cosmogenic* neutrino flux [4, 5]. The detection by the KM3NET collaboration of a muon with an estimated energy of $E_\mu = 120^{+110}_{-60}$ PeV could constitute the first detection of an UHE neutrino [6].

Because they experience negligible attenuation over cosmic distances and are undeflected by magnetic fields, UHENs can act as direct tracers of UHECR sources and can also potentially serve as probes of physics beyond the Standard Model [7, 8]. To date, the UHE neutrino flux Φ_ν above 10 PeV has been constrained to an upper limit of $E_\nu^2 \Phi_\nu \lesssim 10^{-8}$ GeV cm $^{-2}$ s $^{-1}$ sr $^{-1}$ with the possible exception of the recent KM3NET event [9]. This corresponds to a detection rate of less than one event detected per cubic-kilometer per decade for energies above 10 PeV [10, 11]. Consequently, fiducial volumes in excess of $\mathcal{O}(10 \text{ km}^3)$ are required to achieve useful detection rates. Such detector scales are prohibitively expensive for water- and ice-based

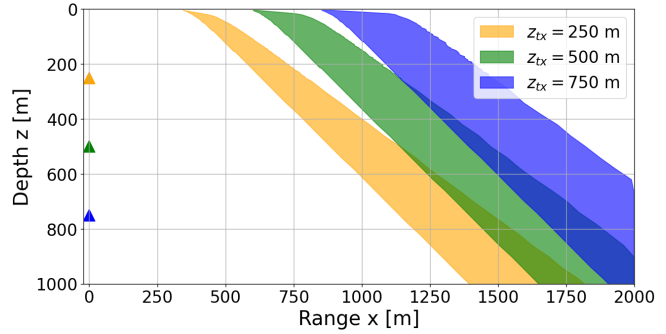


FIG. 1: Radio signals that traverse the upper 15 m of the ice exhibit a seasonal fluctuation of $\mathcal{O}(0.1)$ in received fluence ϕ^E . Shaded regions highlight the portion of the detection region subject to this seasonal effect for the associated neutrino vertex (shown as triangles at $x = 0$, 3 different example vertices shown).

optical Cherenkov arrays such as IceCube, ANTARES, KM3NeT, or Baikal-GVD, necessitating alternative detection paradigms.

One approach is to search for Askaryan radiation: coherent radio emission produced at the Cherenkov angle due to the build-up of excess negative charge in a particle cascade [12]. Askaryan radiation appears to the observer as a broadband radio-frequency pulse with a time width of $\mathcal{O}(\text{ns})$. The attenuation length of radio waves, L_α , in polar ice sheets is $L_\alpha \sim \mathcal{O}(1 \text{ km})$ for frequencies in the 100 MHz to 1 GHz regime [13, 14], allowing an array of receiving antennas embedded in the ice to monitor a volume of $\mathcal{O}(10 \text{ km}^3)$. Multiple such arrays can collectively monitor an area more than an order of magnitude larger than that of existing optical Cherenkov observatories at a reduced cost. The in-ice Askaryan detection method has been field-tested by the RICE [15], ARIANNA [16], ARA [17], and RNO-G [18] experiments. Alternatively, airborne observatories can monitor the ice sheet for Askaryan radiation from high altitudes, achieving greater detection volumes during limited-duration flights. This method was first

* akyriacou@ku.edu

utilized by the ANITA [19] experiment and the recently-completed PUEO flight will also search for UHENs through this method [20]. Although these experiments have not yet detected neutrinos they have refined radio detection techniques, identified sources of background, and established upper limits on the UHE neutrino flux [21–23]. Additionally the ANITA, ARIANNA and RNO-G experiments have observed radio showers induced by cosmic rays [24–26].

A more recently proposed in-ice strategy is the *radar echo method*, in which an array of transmitting antennas broadcasts a radar signal into the ice. The signal is effectively scattered by the ionization trail left in the wake of a relativistic particle cascade. This approach also benefits from the radio transparency and density of glacial ice by allowing monitoring of much larger volumes than possible with optical methods. Radar echo detection of particle cascades was first demonstrated in experiment T576 at SLAC, where a high-energy electron beam was directed into a block of high-density polyethylene, simulating a cascade of similar energy to that produced by an $E_\nu \geq 10^{18}$ eV neutrino interaction. A radar reflection signature correlating with the cascade was subsequently identified in an analysis [27]. The Radar Echo Telescope for Cosmic Rays (RET-CR), which operated during the northern summer seasons of 2023 and 2024, aims to validate this method in natural settings by detecting radar echoes coincident with high-energy cosmic rays recorded by surface scintillator and radio detectors [28, 29]. RET-CR has, at the time of this writing, completed a season of data-taking, and analysis is underway to identify radar echo events.

For both approaches, accurate reconstruction of UHE neutrino events require precise modeling of radio wave propagation between the neutrino vertex and the receiving antennas. Beneath depths of up to $\mathcal{O}(100\text{ m})$ [30, 31], the Greenlandic and Antarctic ice sheets exhibit nearly homogeneous density $\rho_i = 917\text{ kg/m}^3$ [30], and the refractive index has been measured as $n_{i,\text{gr}} = 1.778 \pm 0.006$ in deep Greenlandic ice [32], resulting in straight-line radio propagation. At shallower depths however the ice is characterized by the *firn layer*, a region where snow gradually is compacted into ice. The density increases with depth, causing a velocity gradient in the planar wavefront, which has the effect of *curving* the ray paths of radio signals. Glaciological models and measurements indicate that the firn layer exhibits time-varying fluctuations in both temperature and density [33–35]. This implies that radio signals traversing the firn may experience time-dependent variations in path and amplitude.

The aim of this study is to characterize and quantify, to first order, the magnitude of seasonal variation in firn-traversing radio signals and examine the implications for UHE neutrino reconstruction. We simulate

the propagation of a broadband radio pulse from a hypothetical neutrino interaction vertex within the ice to a receiver array located between the surface and 160 m depth. This simulation is repeated for a series of refractive index profiles derived from firn density measurements at Summit Station, Greenland ($72^\circ 36' \text{ N}$, $38^\circ 25' \text{ W}$; ~ 3200 m a.s.l.) [36], predicted by glaciological models spanning January 1980 to December 2021. The received waveforms are compared across all scenarios to evaluate variations in signal fluence and time-of-flight. Section II describes the data-driven modeling of firn profiles using the Community Firn Model. In Section III, we detail the radio simulation framework. Results are presented in Section IV, and implications for neutrino detection are discussed in Section V.

II. FIRN EVOLUTION AT SUMMIT, GREENLAND

Firn is the transitional stage between fallen snow and glacial ice, with the densification process primarily driven by gravity via the overburden pressure of shallower layers of firn. The rate of densification k is also a function of temperature, and the densification is governed by multiple physical processes [30]. Two processes of particular importance are the initial phase of settling and grain growth that occurs until a threshold density of $\rho_{550} = 550\text{ kg/m}^3$, and a later process known as sintering which becomes dominant beyond this threshold. Sintering is the gradual fusion of distinct ice grains into a continuous bulk as the areas of contact expand due to sublimation and vapor transport of water molecules [30, 37]. The former process is faster and exhibits greater sensitivity to temperature than the latter. At greater depths, past a threshold density of $\rho \approx 800 - 840\text{ kg/m}^3$, the densification is dominated by the compression of the remaining pores by the overburden pressure. Generally, the firn density profile $\rho(z)$ in the polar regions can be approximated using an asymptotic exponential decay function of depth z (where $z > 0$ is below the surface and $z < 0$ is above the surface) approaching the density of ice ρ_i :

$$\rho(z) = \begin{cases} \rho_i + (\rho_s - \rho_i)e^{-k_0 z} & \text{if } \rho \leq \rho_{550} \\ \rho_i + (\rho_{550} - \rho_i)e^{-k_1(z - z_{550})} & \text{if } \rho > \rho_{550}, \end{cases} \quad (1)$$

With $\rho_s = \rho(z = 0)$ being the surface density, k_0 and k_1 corresponding respectively to the densification rate above and below the inflection depth z_{550} where the threshold density ρ_{550} is reached. Hereafter the region between the surface and z_{550} is defined as the *shallow firn* and the region between z_{550} and z_{820} (the depth at which $\rho = 820\text{ kg/m}^3$) is defined as the *deep firn*, with the depth below defined as the *glacial ice*. It is also possible to model the firn's density profile with a three-part asymptotic exponential, with an additional densification rate k_2 beyond the pore close off threshold

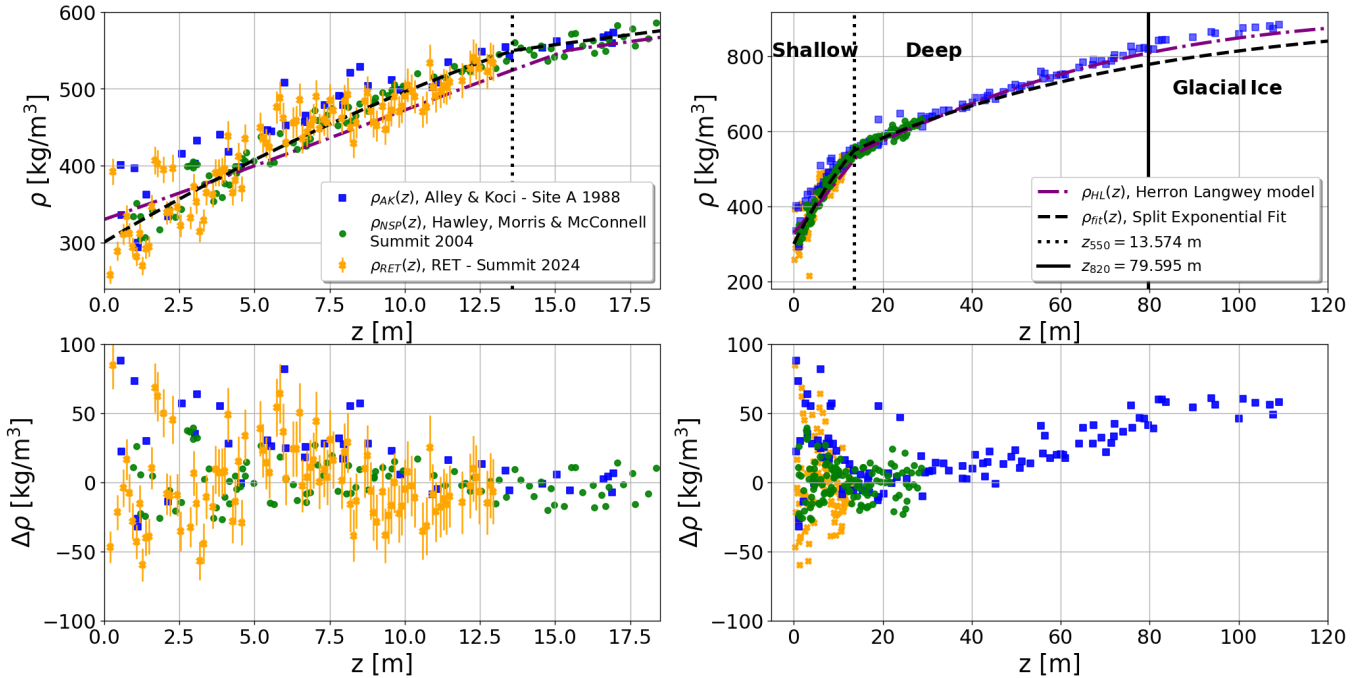


FIG. 2: Top: Two measured density profiles at Summit; $\rho_{RET}(z)$ [38] & $\rho_{NSP}(z)$ [39], alongside a density profile $\rho_{AK}(z)$ made at Site A [40], located 222 km south of Summit station. A split asymptotic exponential function $\rho_{fit}(z)$ is fit to the NSP (Neutron Scattering Probe). The output of the Herron-Langway $\rho_{HL}(z)$ model is also shown. The left plot zooms in to the shallow firn $z < 15$ m, where the fluctuation in density is most pronounced, and shows the measurement uncertainties for the RET data. The right displays density profiles down to the glacial ice. Bottom: The residuals of the measured density profiles to the best-fit function.

depth z_{820} [41]. However as this study is concerned with seasonal changes in the firn which take place at shallower depths and due to the constraints with the glaciological modeling software, we instead utilize the two component exponential model, referred to hence as the *double exponential model*. One can derive an asymptotic exponential density dependence on depth using the Herron-Langway (HL) model [42], with an assumption of constant accumulation and temperature. Various physical models are used to estimate firn density evolution with time-variant temperature and accumulation rates, but for the most part are extensions upon the Herron-Langway model [43] and are discussed in greater detail in Appendix A.

In Fig. 2 we show two density measurements of the firn in the vicinity of the Summit site, alongside a separate measurement of the firn at another location on the central Greenlandic ice shelf known as Site A at a similar elevation. The first of these datasets illustrated is the density profile $\rho_{NSP}(z)$. This was measured in June 8th, 2004 to a depth of 30 m approximately 1 km from the main camp at Summit station, utilizing a neutron scatter probe (NSP) lowered into a borehole, which reconstructed the density from the return scatter of neutrons emitted by a radioactive source [39, 44]. The measurement uncertainty was not explicitly defined,

but the authors stated that an error of $\delta\rho/\rho \approx 6\%$ is expected for a probe centered borehole of a diameter of 12 cm [39], whereas the borehole used has a diameter of ≈ 14.1 cm [45]. We then show a direct density measurement of ice cores $\rho_{AK}(z)$ made in 1988 to a depth of 120 m at Site A $70^{\circ}45'N$, $35^{\circ}57.5'W$; 3145 m a.s.l.) located approximately 222 km south east of Summit [40]. Finally a direct measurement of the density ρ_{RET} to a depth of 13 m at the RET-CR deployment site in May of 2024 [38]. Cores were taken with a coring drill, trimmed to ensure consistent density, and then sliced to a uniform thickness of 10 cm, and therefore constant volume, to be weighed. In this case, cores were extracted using a coring drill, trimmed to ensure consistent geometry, sliced to a uniform thickness of 10 cm, and weighed to determine density. Snow chips produced during cutting (corresponding to $\sim 2.2\%$ of the core volume) were included in the mass measurement, though some loss due to wind is expected. Accounting for chip loss and possible core misalignment, we conservatively estimate a relative density uncertainty of $\delta\rho/\rho \lesssim 4.4\%$, superseding a larger estimate ($\delta\rho/\rho > 7\%$) reported in earlier proceedings [38].

All three datasets are shown alongside a split exponential function made as a best fit to $\rho_{NSP}(z)$, as well as the residuals of the data relative to the fit. The best

fit parameters are:

- $\rho_s = 300 \pm (5 \cdot 10^{-3}) \text{ kg/m}^3$,
- $k_0 = (38.2 \pm 13) \cdot 10^{-3} \text{ m}^{-1}$,
- $k_1 = (14.8 \pm 2.2) \cdot 10^{-3} \text{ m}^{-1}$,
- $z_{550} = 13.56 \pm 0.69 \text{ m}$.

Also shown is the density profile $\rho_{\text{HL}}(z)$ predicted by the Herron–Langway model, evaluated using an average firn temperature of $T = -31.4^\circ\text{C}$, an accumulation rate $A = 0.23 \text{ m yr}^{-1}$ (ice equivalent), and a surface density $\rho_s = 350 \text{ kg m}^{-3}$ [42]. Notably, this model predicts the change of densification processes to occur at slightly deeper depth of $z_{550} = 14.9 \text{ m}$. The three datasets each show increasing density with depth, with residuals to the exponential fit generally lying within $|\Delta\rho| < 50 \text{ kg/m}^3$, with some notable ‘over-fluctuations’ in excess of $|\Delta\rho| > 50 \text{ kg/m}^3$. These include an apparent dense layer at $z \approx 2 \text{ m}$ and at $z \approx 6 \text{ m}$ in the RET density profile, and numerous over-fluctuations in the in Site A data. We see as that the Site A data is more consistent with the Herron–Langway model at $z > 60 \text{ m}$ than the exponential function fit to the NSP data.

While all three datasets exhibit a consistent increase in density with depth, the residuals reveal substantial small-scale density variability in the near-surface region ($z \lesssim 5\text{--}10 \text{ m}$), with fluctuations frequently reaching $|\Delta\rho| \sim 10\text{--}50 \text{ kg m}^{-3}$ and occasional larger excursions. This enhanced shallow variability is observed across independent datasets and measurement techniques, suggesting that it reflects real variability in the firn density.

A. Modeling Firn Evolution

To obtain a realistic estimate of the evolving firn density profile $\rho(z, t)$ at Summit Station, Greenland, we used glaciological simulation software known as the ‘Community Firn Model’ (CFM) [43]. CFM is a modular code that models the physical and chemical properties of a volume of firn and how they change over time, including, but not limited to the: density profile, temperature profile, age of each layer, concentration of isotopes and water content [43]. CFM can model changes in the properties in response to changing air temperature, surface accumulation, changing surface density, melt events, and other factors. CFM uses a Lagrangian grid with a fixed number of volumes, each corresponding to a layer of firn with identical properties. At each iteration i , a new layer is added to the top, corresponding to newly accumulated snow over the time interval Δt_i , and the deepest simulated layer is removed from the bottom. The density profile is evolved from $\rho(z, t_i)$ to $\rho(z, t_{i+1})$ using the specified densification equation, with changes in temperature, melt-water

concentration, and overburden pressure being forced from the surface.

For this study, the CFM simulation was initialized at January 1980 with an initial firn model, with the starting density profile $\rho_0(z) = \rho_{1980,1}(z)$ estimated using the Herron–Langway model, with the mean annual temperature of $T = -31.4^\circ\text{C}$ and accumulation rate of $A = 0.23 \text{ m/yr}$ (ice-equivalent) acting as inputs. The density profile for each year y and month m is designated as $\rho_{y,m}(z)$. The model domain extends down to $z = 120 \text{ m}$, with a depth binning of $\Delta z = 0.01 \text{ m}$. Below 120 m the depths are estimated using a best-fit asymptotic exponential function as shown in Equation 1. The time interval Δt_i is one month and the final iteration is December 2021. The surface density was held constant at a value of $\rho_s = 350 \text{ kg/m}^3$. For each iteration, the monthly averaged accumulation rate A_i , skin temperature T_i , and the sum of melt-water volume, is obtained from MERRA-2 data[46]. We utilized the Kuipers–Munneke (KM) densification model to define the densification rate for each time step following the initialization [47]. The KM model has been widely validated and used for Summit Station, Greenland, and provides a physically based description of dry-snow compaction suitable for modeling long-term firn evolution under cold, low-melt conditions [43].

A density profile $\rho_{y,m}(z)$ is therefore calculated for each time step, allowing a set of refractive index profiles $n_{y,m}(z)$ to be calculated using the empirically derived relationship between n and firn density ρ [48]:

$$n(z) = 1 + 0.845 \frac{\rho(z)}{\text{g/cm}^3}. \quad (2)$$

B. Results for Density and Temperature

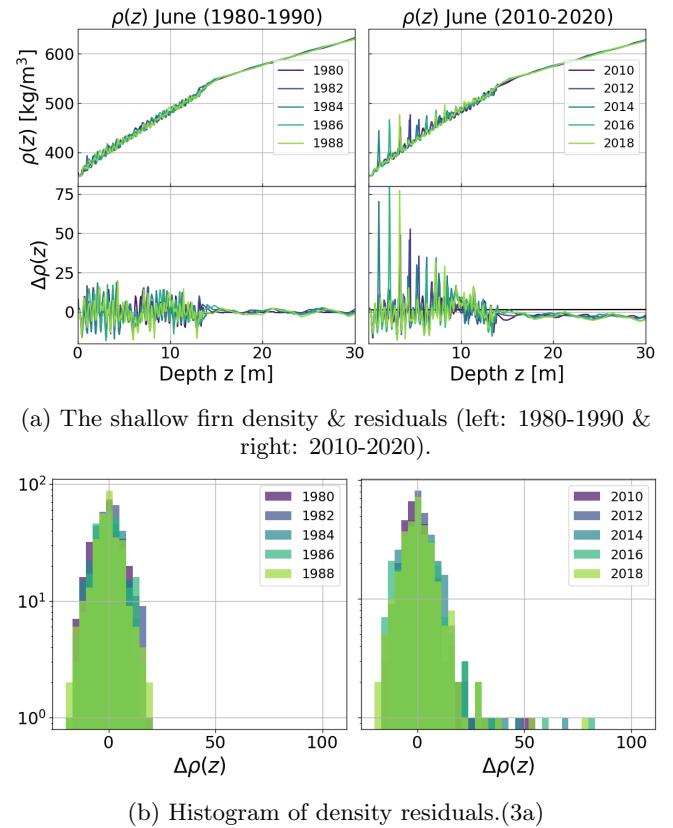
Using the MERRA-2 data inputs, the firn temperature, melt-water concentration, water run-off, and isotope concentrations were computed as a function of depth for each simulated epoch. The temperature for shallow depths of $z < 10 \text{ m}$ undergoes a seasonal oscillation, with a maximum surface temperature of -5°C to -10°C in July to a minimum of approximately -50°C in February. The temperature oscillation propagates deeper into the ice while undergoing dampening, with an isothermal depth at $\approx 10 \text{ m}$, a result in good agreement with field measurements of the firn temperature at Summit [44]. To quantify the density fluctuation, we define density residuals $\Delta\rho_{y,m}(z)$, which are defined with respect to the starting profile $\Delta\rho_{y,m}(z) = \rho_{y,m}(z) - \rho_{1980,1}(z)$.

For the shallow firn ($z < 15 \text{ m}$), one can classify ‘small scale’ density fluctuations with $|\Delta\rho| < 25 \text{ kg/m}^3$, that are present across the entire simulated data set and ‘large scale’ density fluctuations $|\Delta\rho| > 25 \text{ kg/m}^3$ that are

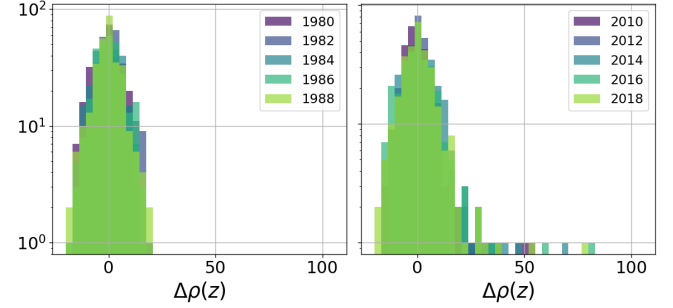
prominent from the year 2000 onward. The large scale density fluctuations correspond to surface melt events, which we discuss in more detail below. The residuals of the small-scale fluctuations obey a Gaussian-like distribution, with a least-squares fit yielding a standard deviation $\sigma_{\Delta\rho,CFM}(z < 15 \text{ m}) = 7.24 \text{ kg/m}^3$ and a mean $\mu_{\Delta\rho,CFM}(z < 15 \text{ m}) = 0.078 \text{ kg/m}^3$ for the decade of 1980-1990, as shown in Fig. 3b. The small-scale fluctuations are a result of the seasonal temperature oscillation in the upper 10 m of the firn. The large-scale fluctuations act as outliers from this distribution, with $\Delta\rho$ reaching values of $\Delta\rho = 60 - 100 \text{ kg/m}^3$ shown in Fig. 3b. For the deep firn, the density residuals are smaller, with a standard deviation of $\sigma_{\Delta\rho,CFM}(z > 15 \text{ m}) \approx 1.1 \text{ kg/m}^3$. The situation for the decade of 1990-2000 resembles that of 1980-1990, with an absence of large melt events, whereas the subsequent decade of 2000-2010 more resembles that of 2010-2020, with melting events occurring in 2002 and 2004.

In the CFM modeling, large-scale fluctuations form within 0.4 m of the surface in correlation with surface-melt events, as the melt water percolates down into the snow and refreezes once the surrounding temperature drops below freezing. With typical densities of $400 - 550 \text{ kg/m}^3$ these refrozen layers persist inside the shallow firn at relatively constant densities at progressively deeper depths as snow accumulates above them, acting as a record of past melt events until they arrive at a depth where the surrounding firn's density matches that of the layer. The formation and deepening of the ice layers are visible in Fig 4, where a color-map of the time-dependent density profile $\rho(z, t)$ is displayed. For example, a 'refrozen' layer forms at $z = 0.3 \text{ m}$ in the June 2002 profile, and by June 2020 is visible at a depth of $z = 9.1 \text{ m}$. The four largest surface-melt events in the dataset by melt volume, occurring in the summer months of 2002, 2004, 2012, and 2019 (the latter featuring a rain event at Summit), correspond to the densest refrozen layers.

For a point of comparison, we consider the density data measured using a neutron scattering probe (NSP) to a depth of 30 m as shown in Fig. 2. Large-scale density residuals of $-20 \text{ kg/m}^3 \lesssim \Delta\rho_{HM} \lesssim 50 \text{ kg/m}^3$ are observed relative to the best-fit in the upper 8 m, while below $z = 15 \text{ m}$, the residuals obey a Gaussian distribution with a standard deviation of $\sigma_{\Delta\rho,NSP}(z > 15 \text{ m}) = 4.95 \text{ kg/m}^3$. Larger density fluctuations are observed in the Alley-Koci and RET density profile. This suggests a higher degree of density variation for the deep firn than implied by the CFM simulation, although the measurement uncertainty of the NSP profile was not stated in the study but is typically on the order of $\delta\rho/\rho \sim 0.02 - 0.05$ [39]. Nevertheless, the NSP data suggests that the magnitude and characteristics of the density fluctuation estimated by CFM are realistic and perhaps conservative compared



(a) The shallow firn density & residuals (left: 1980-1990 & right: 2010-2020).



(b) Histogram of density residuals.(3a)

FIG. 3: The CFM-modeled density profile at Summit for June for the decades 1980-1990 and 2010-2020, with the residuals displayed in profile and in histogram (3b).

to real-world conditions.

III. SIMULATING RF PROPAGATION THROUGH THE FIRN

Having modeled the seasonal variation in the refractive index, we produced a set of refractive index profiles, $n_{y,m}(z)$, which were then used to generate simulated radio propagation data using the aforementioned Kovacs relation between density and refractive index described by Eq. 2 [48].

A. RF Simulation Methods

To examine the resulting variation in radio signal properties, we solved Maxwell's equations numerically across the entire simulation domain and sampled the signal at discrete receiver positions. These simulations were performed using the open-source code **MEEP** [49], a versatile Finite Difference Time-Domain (FDTD) solver. FDTD operates by discretizing the simulation geometry into a grid of cells, within which Maxwell's equations are solved in discrete time steps. Boundary conditions were

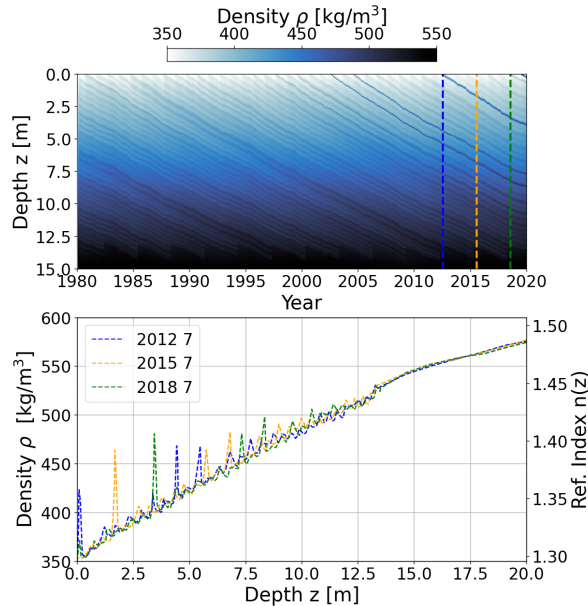


FIG. 4: Above: A color-map of the time-dependent density profile of the shallow firn from 1980 through to 2020. The coloured lines indicate the CFM refractive index model outputs $n_{x,7}(z)$ for month 7 of 2012, 2015 & 2018, which are some of those used to quantify the RF signal variation. Below: shows the discrete density profiles of the aforementioned dates.

implemented using a radiating dipole source initialized at $t_0 = 50$ ns and perfectly matched absorbing layers at the edges of the domain to prevent artificial reflections. Given the high level of accuracy of FDTD methods, our conclusions are largely based on the **MEEP** simulation outputs.

We additionally utilized the parabolic wave equation (PE) method, solved using the simulation code **paraPropPython** or simply **paraProp**. The PE method is based on the parabolic approximation of Maxwell's equations, assuming cylindrical symmetry in the medium and a vertically polarized and monochromatic electric field $E_z(r, z, \omega)$ propagating from the source outwards in the radial direction and assuming a $e^{i\omega t}$ time dependence [50]. Using a step-wise spatial solver, the field $E_z(r, z, \omega)$ is solved throughout the entire geometry. Time-domain solutions can be obtained by repeating this process across the frequency domain of the source signal. The PE method, as implemented in **paraProp**, provides accurate radio solutions within a paraxial angle $\theta_{paraxial} = 45^\circ$ relative to the radial direction of the domain and has been verified against FDTD codes within geometries comparable to that used in this study [50]. The greater simulation efficiency of PEs compared to FDTD allows solutions to be computed on time scales that are orders of magnitude smaller, allowing for the possibility of Monte-Carlo-type analyses and the

simulation of larger simulation domains than possible for FDTD methods.

Finally, numerical ray tracing (RT) was used to approximate the path taken by RF signals from source to receiver, allowing us to discern useful information such as the arrival angle of different signals at receivers, independently check if the signal has undergone reflection or refraction and the portion of the signal's travel path spent in different zones of the ice. The **SignalProp** module of the **NuRadioMC** code was used to generate ray tracing solutions for given pairs of sources and receivers, utilizing the **radioprop** solver [51, 52]. The RT solutions used throughout Sections IV and V were solved using the best fit of the double exponential model (described in Eq. 1) to the CFM profile corresponding to January 2010, with the parameters and the profile described in the Appendix E.

B. Geometry and Source Modeling

The simulation geometry was assumed to be cylindrically symmetric, reducing the problem to two dimensions: radial distance x and depth z . This choice, taken to minimize computational costs, can be justified by invoking the relatively flat terrain at Summit, the absence of large crevasses that can act as planar reflectors, and the rapidly diminishing power of pipe-like and point-like reflectors, with the power P_{rx} diminishing with distance L described with $P_{rx} \propto L^{-3}$ & $P_{rx} \propto L^{-4}$ respectively. The ice-air boundary was defined as perfectly flat at $z = 0$, with air occupying the region $z < 0$ and ice at $z \geq 0$. The geometry consists of two distinct regions: an ice cylinder extending to a radius of $X_{ice} = 520$ m and depth of $Z_{ice} = 200$ m, with a refractive index profile given by the corresponding $n_{y,m}(z)$; an overlying air cylinder of homogeneous refractive index $n = 1$ with the same radial extent and a height of $H_{air} = 10$ m.

To exclude any artificial reflections caused at the edges of the simulation domain, an outer 'buffer' radius of 30 m is defined, since **MEEP** is not able to define a perfectly matched layer (PML) perpendicular to the radial direction when using cylindrical symmetry. As a further precaution from artificial reflections, two buffer layers of width 40 m were used for the upper and lower edge of the domain respectively, in addition to a 40 m PML layer applied to the top and bottom side of the respective buffer layers. The computational grid had a cell size of $\Delta x_{cell} = 0.033$ m, resulting in a FDTD time step of $\Delta t = 0.056$ ns. As the in-simulation sampling rate is higher than that of radio neutrino experiments, only every 5th time step was sampled and recorded, resulting in an effective sampling rate of 3.6 GHz and sampling time interval of 0.28 ns. Given the simulation's resolution and size specifications, frequencies above

$\Delta\theta_{VC}$ [°]	f_{low} [GHz]	B [GHz]	f_{max} [GHz]	t_{FWHM} [ns]
3.5	0.076	0.53	0.167	3.07
5.0	0.056	0.37	0.120	4.31
7.5	0.038	0.25	0.82	6.41

TABLE I: The spectral properties of the transmitted signal (using different inputs of $\Delta\theta_{VC}$): the low cutoff frequency f_{low} , the bandwidth B , the frequency of maximum amplitude f_{max} , and the FWHM spread of the pulse t_{FWHM} . The corresponding pulses and spectra are displayed in Fig. 5.

0.5 GHz experienced noticeable numerical dispersion, so the usable signal spectrum was limited to well below this threshold when using FDTD. The in-simulation time-window has a length of $t_{max} = 3200$ ns, ensuring that all signal arrivals and their relevant decay tails were captured at the receiver locations.

The emission of a band-limited RF impulse was simulated from a short dipole source located at a depth z_{tx} within the ice as a test pulse. The frequency dependence of its spectrum follows the Alvarez-Muñiz-Zas (AMZ) parametrization for the Askaryan spectrum of a $E_{sh} = 10^{18}$ eV hadronic shower, viewed at an angle offset by $\Delta\theta_{VC} = |\theta_V - \theta_C|$ from the Cherenkov angle [53], referred to hereafter as the viewing-angle offset. This parameterization is used here solely as a form factor to define a relatively ‘Askaryan-like’ pulse envelope; we do not explicitly model the cascade nor the near field emission. To explore the wavelength dependence of ice-induced signal modulation we utilized spectra with viewing angle offsets $\Delta\theta_{VC} = 3.5^\circ$, 5.0° and 7.5° , respectively. As the viewing angle deviates further from the Cherenkov angle, the coherence breaks down for successively longer wavelengths and the signal power diminishes, leading to the successively narrower and dimmer spectra seen in Fig 5. Given the aforementioned issue of numerical dispersion in FDTD, only the latter signal ($\Delta\theta_{VC} = 7.5^\circ$) is used in the MEEP simulations whereas all 3 are utilized to initialize the paraProp simulations. The emitted signal for $\Delta\theta_{VC} = 7.5^\circ$ has a bandwidth of 156 MHz, with a 3 dB lower frequency cutoff at $f_{low} = 19$ MHz and a high frequency cutoff at $f_{high} = 175$ MHz, and a maximum spectral power at $f_{max} = 82$ MHz. The resulting pulse has a full width half-maximum (FWHM) time spread of $t_{FWHM} = 6.41$ ns, with the pulse and spectrum shown in Fig. 5. The low frequency cutoff f_{low} , frequency maximum amplitude f_{max} , bandwidth B , and FWHM time spread t_{FWHM} of the signals for the different observer angles are listed in Table I. As the source was modeled as a short dipole antenna, a single simulation run was able to illuminate most of the receiver array, allowing the investigation of ice-induced propagation effects across a broad range of paths.

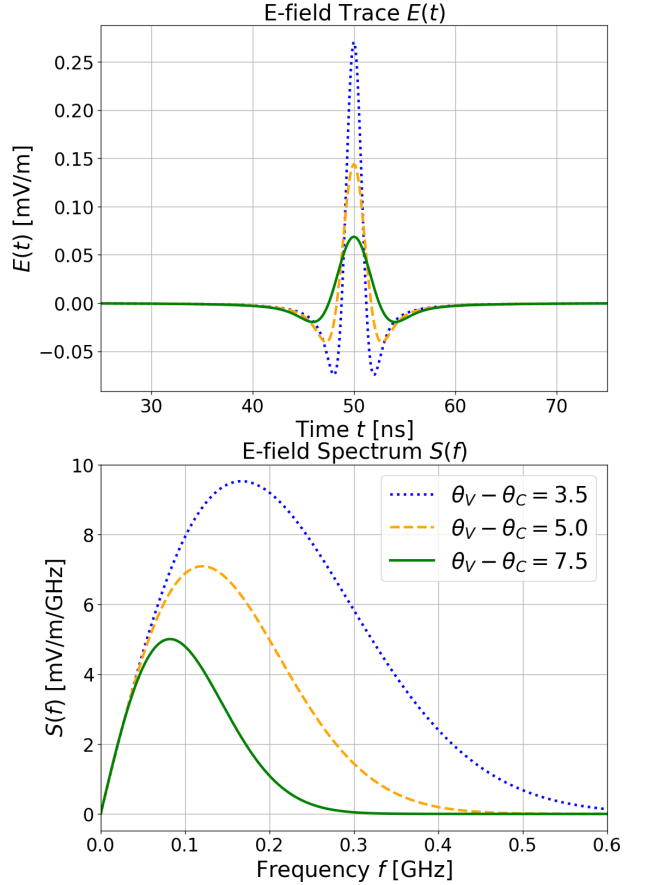


FIG. 5: The test pulses (top) & spectra (bottom) injected into the source in the RF simulations, with the former initialized such that the amplitude maximum occurs at $t_0 = 50$ ns. The spectra are modeled using the AMZ parameterization of a hadronic shower observed from viewing-angle offsets of $\Delta\theta_{VC} = |\theta_V - \theta_C| = 3.5^\circ$, 5.0° & 7.5° [54]. Parameters such as the bandwidth and time spread of the pulses are summarized in Table I.

The transmitted pulse was sampled at an array of receivers positioned at radial distances x_{rx} ranging from 160 m to 520 m in increments of $\Delta x_{rx} = 10$ m, and at depths z_{rx} from 4 m to 160 m in increments of $\Delta z_{rx} = 4$ m. These receiver positions were chosen to match the depths sampled by past and existing radio and radar neutrino detectors, including ARIANNA, RNO-G, RET-CR, as well as the proposed depths of the IceCube-Gen2 Radio Array. The computational restraints prevented us from simulating these effects at depths $z_{rx} > 160$ m, utilized by the RICE and ARA detectors, so we use ray-tracing arguments to extrapolate our results to greater depths.

For simplicity, each refractive index profile $n_{y,m}(x, z)$ was assumed to be range-independent, such that

$n_{y,m}(x, z) = n_{y,m}(z)$. Although this does not reflect the true horizontal variability present even in extremely cold environments such as Summit Station or the South Pole, it offers a useful approximation for isolating vertical profile effects. The refractive index profiles were discretized with a vertical resolution of 0.1 m, finer than the shortest simulated wavelength $\lambda_{min} \approx 0.33$ m, ensuring accurate representation of refractive index gradients within the simulation. Finally, the refractive index was modeled with no imaginary (conductive) component, and thus we assume no dielectric attenuation across the domain.

C. Signal Observables

Given an ice model described by the two-part exponential function expressed in Eq. 1, the received signal is composed of two pulses: a primary pulse traveling from the source to the receiver which arrives earlier and generally has a larger amplitude, and a secondary pulse that arrives later, generally has a lower amplitude owing to its greater travel path.

The latter has been reflected by the air-snow interface at the surface, leading to an inversion of polarity and further amplitude decay via transmission loss, or has been refracted without reaching the surface. Indeed, for most of the receiver domain, the signal power is overwhelmingly composed of two pulses which correspond to these two paths through the firn and ice. In keeping with convention, we describe the primary, least-time signal as ‘direct’ even though it may have undergone refraction along its trajectory. This simple bi-pulse description does not hold true within the so-called shadow zone where emission is forbidden under classical ray tracing, discussed in greater detail in the following section. Outside the shadow zone, the primary and secondary pulses are referred to as ‘D signals’ and ‘R signals’ respectively. We define the following signal parameters to characterize our simulated signals:

- Propagation times of the D and R signals: t_D [ns] & t_R [ns]: The time of maximum amplitude of the D and R signals (rather than signal onset time),
- Time delay $\Delta t_{DR} = t_R - t_D$ [ns]: The relative propagation time delay between t_D and t_R ,
- Fluence: $\phi^E = \epsilon c \int_{t_0}^{t_1} E_{RX}(t)^2 dt$ [eV/m²]: The integrated RF energy flux between times t_0 and t_1 , with ϵ being the absolute local permittivity and c being the speed of light.

The fluence ϕ^E can be estimated for the entire waveform or can be estimated independently for the D signals and R signals, allowing us to disentangle effects from different components of the ice-sheet. Hence we will define ‘total fluence’ ϕ_{tot}^E as distinct from the fluence of the individual

D signal ϕ_D^E or R signal ϕ_R^E . The D fluence ϕ_D^E is integrated over the time window $t_D - t_{res}$ ns to $t_D + t_{res}$ ns. Here t_{res} is set to a value of $t_{res} = 2t_{FWHM} = 12.82$ ns, selected to correspond to twice the FWHM time spread of the source pulse generated for a viewing-angle offset of $\Delta\theta_{VC} = 7.5^\circ$. The same time window is used to calculate ϕ_R^E by integrating about t_R .

To identify the D and R pulses for a given RX position, we find the time of the two brightest peaks in the Hilbert transform of the waveform. If ray tracing (RT) predicts two solutions for the RX, and if the peaks are separated by at least $t_{res}/2$, we designate the time of the earliest peak as t_D , and the following peak as t_R . If RT predicts only one solution (such as near the shadow zone boundary), or no solutions, then the time of brightest emission of the waveform is designated t_D . We caution the reader that while we define the brightest signal as the D signal for all cases where an R signal can not be identified with ray tracing, this relationship is not necessarily true in the shadow zone. Furthermore, we define another region of the geometry as the ‘overlap’ region; where ray tracing predicts two solutions such that $\Delta t_{DR} \leq t_{res}$. In this region, the inherent spread of the pulses generally results in overlap and interference between the D and R pulses, meaning that the variation in time of flight and fluence can not be viewed in isolation for the two propagation paths. Thus, one must be cautious to interpret the results for time and fluence variation within the shadow and illuminated zones.

To quantify the magnitude of variation in the signals from different times for signal parameter x_i for refractive index scenario $n_{y,m}$, we calculate the *variation coefficient* $\delta x/x$:

$$\frac{\delta x}{x} = \frac{\sigma(x)}{\mu(x)}, \quad (3)$$

Where $\mu(x)$ is the mean parameter of x across all CFM scenarios and $\sigma(x)$ the standard deviation. Given that fluence can vary by orders of magnitude in our simulation domain due to propagation losses, it is prudent to examine the variation coefficient which we also refer to as the *relative variation*, as outlined in Section IV C 1. In other cases, we examine the seasonal distribution of the relative fluence residuals at specific receivers. In Section IV C 2, we examine the *absolute variation* of the absolute propagation times $\delta t = \sigma(t)$ for the D and R signals and their relative offset Δt_{DR} .

IV. RESULTS

The principal result of this study is that seasonal density fluctuations in the firn produce the strongest variation in received RF fluence along shallow refracted paths, while direct and deep-reflected signals remain comparatively stable. In contrast, the impact on signal ar-

rival times is generally on a scale of nanosecond or sub-nanosecond scale outside of the shadow zone. As will be demonstrated in Section V, the variation in both quantities result in uncertainty in neutrino reconstruction.

A. Propagation Domains

The degree and nature of seasonal fluctuation in received RF signals differs considerably depending on the relative position of the receiver to the transmitter, and hence on the path taken by the signal through the ice according to ray tracing. To illustrate this, we divide the receivers by depth into *shallow* receivers and *deep* receivers, the former located at $z_{rx} < 15$ m and the latter at $z_{rx} > 15$ m. We further divide the deep geometry by depth and range into three distinct propagation zones as defined by ray tracing; the *reflection*, *refraction* and *shadow* zones.

Signals observed by deep receivers in the reflection and refraction zones are characterized by the two signal components; the primary (D) signal, which may propagate in a straight line or may have had its path curved through refraction, followed by the secondary signal (R) that is either reflected off the ice-air interface, or undergoes refraction above the depth of the receiver. The reflection zone extends from the surface to the deepest reaches of the ice, and extends from the transmitter range $x_{tx} = 0$ to the critical reflection boundary described by a range $x_L(z)$. Beyond this boundary is the refraction zone, where the secondary signal propagates from the source in an up-going arc but is refracted to a down-going trajectory before it can reach the surface, instead reaching a minimum depth or depth of closest-approach to the ice-air interface. It is instructive to subdivide this zone into the shallow and deep refraction zones, where the secondary signal's closest approach to the surface is within the shallow firm and below it, respectively.

The separation between the shallow and deep refraction zones is hence designated by the *shallow refraction boundary* range $x_{R,15}(z)$. Beyond the *shadow boundary* $x_S(z)$ is the shadow zone, where no valid ray path is permitted under classical ray tracing. In fact, shadow zone RF signals have been observed in multiple field experiments and, in the presence of density fluctuations, are predicted in this zone by FDTD and PE simulation methods, including in this study [50, 55]. We will also refer to the aforementioned 'overlap region' where the time between the primary and secondary is less than or equal to twice the FWHM spread time of the pulse; this region is dependent on the spectrum of the pulse but not on its propagation as defined by RT.

1. Fluence by domain

To display the characteristics of the RF signal in the different propagation zones, in Fig. 6 we show heatmaps of the signal fluence ϕ^E for the 2015 January firm model $n_{2015,7}(z)$ the primary fluence ϕ_D^E in Fig. 6a and the secondary fluence ϕ_R^E in Fig. 6b. The latter heatmap excludes the shadow zone by construction due to the breakdown of a simple 'bi-pulse' model in the shadow zone, the former simply defines the brightest peak in the waveform as being associated with the primary signal. A refrozen ice layer located at $z \approx 2$ m is a major feature of $n_{2015,7}(z)$, as shown in Fig. 4. The critical reflection boundary $x_L(z)$, the shallow refraction boundary $x_{R,15}(z)$ and the shadow zone boundary $x_S(z)$ are also indicated using lines. The shadow zone is evident as a dark region in the top right of Fig. 6a, where the fluence is reduced by at least two orders of magnitude compared to the non-shadow zone, but non-zero. Relatively bright fluence 'hot-spots' are present between the shadow zone boundary and are clearly evident in both maps. As these are contained within the 'overlap' region, it is possible that we are seeing artificial enhancement of the D and R fluence due to positive interference between the distinct pulses. This boundary band may also be associated with the inflection point in the refractive index at $z_{550} = 14.9$ m, causing multiple parallel ray-paths to constructively interfere. Between the reflection and shallow refraction boundaries, there are bands of relatively high fluence visible in Fig. 6b, with the peak fluence at $z = 160$ m located at a range $400 \text{ m} < x < 420$ m and the other brighter band's peak located at ranges $450 \text{ m} < x < 500$ m. These bands suggest constructive and destructive interference within the shallow refracted zone resulting from the presence of the refrozen layer at $z \approx 2$ m.

B. Signal Variation

We examine the change in the characteristics of the pulses in the different propagation regions by showing example waveforms at ranges of $x_{rx} = 160$, and 350m (designated A and B respectively) and at depths of $z_{rx} = 8$ m (shallow) and at 100 m (deep).

1. Shallow Receivers

Waveforms within the shallow firm experience notable lensing effects due to the presence of over-dense layers. These layers can also give rise to second-order reflections, so that waveforms in this domain may have more than two components. The pulses received at $z_{rx} = 8$ m are shown in Fig. 7 alongside their spectra and the spectrum of the source signal scaled to the maximum amplitude of the brightest signal. The simulated outputs from the ice models $n_{2010,7}(z)$, $n_{2012,7}(z)$, $n_{2015,7}(z)$, and $n_{2018,7}(z)$

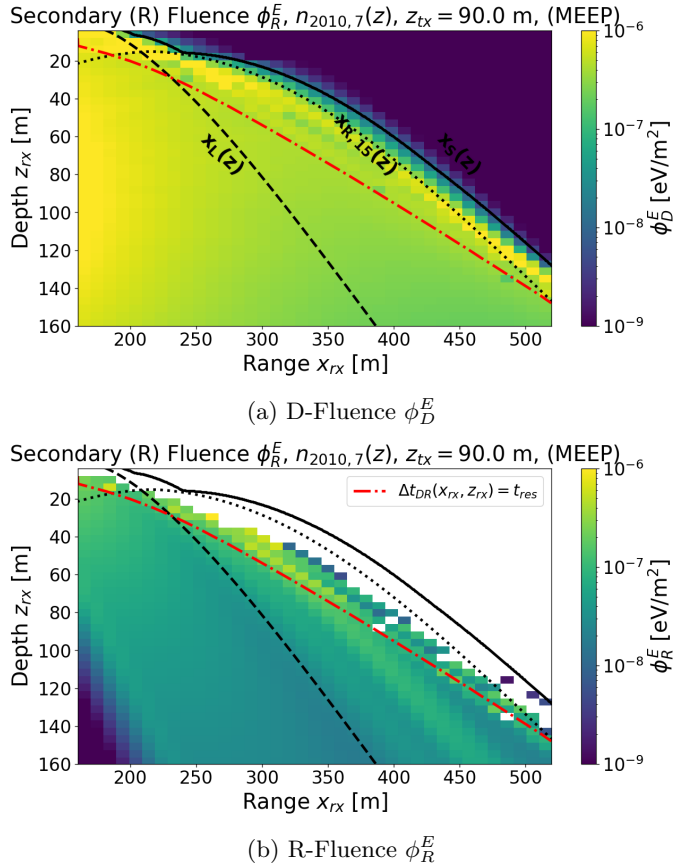


FIG. 6: A heatmap showing the received signal fluence ϕ^E (a: total, b: D signal, R signal) as a function of receiver position with spline interpolation, from a source at $z_{tx} = 90$ m propagating through the refractive index profile $n_{2015,7}(z)$. The different propagation regions are indicated with the boundary lines x_L , $x_{R,15}$ and x_S . An additional line indicates the overlap region where the D and R signals have a relative delay of $\Delta t_{DR} < t_{res} = 12.82$ ns.

are overlaid. Whereas receiver A is located within the illuminated regime, receiver B falls within the shadow zone, and their signals are therefore significantly attenuated relative to A and cannot be described by a simple double-pulse model. Receiver A exhibits a clear primary pulse with normal polarity at $t_D = 998$ ns that partially overlaps with a secondary, inverted pulse peaking at 1010 ns. Likewise, spectra at receiver A show similar shapes, with 4 distinct peaks owing to the combination of the spectra of the D and R signals. The amplitude of these peaks vary on the order of a few percent. Across the different ice models, the resulting fluence fluctuations reach 4.47%, while arrival-time fluctuations remain below the sub-ns level. Receiver B, in contrast, shows a complex dispersive structure spanning 1800–2500 ns that varies in overall fluence and shape. The spectra at receiver B do not well match the shape of the origin, being composed of a large number of peak structures that are indicative

of the combination of multiple wavelets. The attenuated and broadened waveform at receiver B (1900–2500 ns) exhibits long-lived oscillatory tails whose morphology differs between ice models, highlighting the sensitivity of shadow-zone propagation to small seasonal variations in the firn profile.

2. Deep Receivers

Fig. 8 shows the simulated pulses and spectra recorded at receivers located at $z_{rx} = 100$ m for horizontal baselines of 160 m and 350 m, once again labeled A and B respectively. Figures 8a, 8b, and 8c illustrate the full received waveforms, the primary (D) waveforms and spectra, and the secondary (R) waveforms and spectra, respectively, with results from the ice models $n_{2010,7}(z)$, $n_{2012,7}(z)$, $n_{2015,7}(z)$, and $n_{2018,7}(z)$ overlaid. For comparison, the spectrum at the source is overlaid against the RX spectra, and scaled such that the displayed spectral maximum is a factor of 1.1 times greater than maximum amplitude of the brightest RX signal. In Fig. 8a, the full waveforms display the expected trend of pulse broadening and attenuation with increasing baseline. The receiver at 160 m detects a sharp double-pulse structure with amplitudes of order 10^{-8} V/m, while at 350 m the signals are delayed and more dispersed, with amplitudes reduced by one to two orders of magnitude. Fig. 8b isolates the primary D-pulse, showing that across all three baselines, the arrival times are consistent to the sub-ns level between ice models. At $x = 160$ m, the D-pulse appears clean and symmetric, whereas at $x = 350$ m the pulse shape becomes increasingly broadened, though the peak amplitudes remain stable across years. Fig. 8c presents the secondary (R) pulse components. These exhibit greater variation between ice models than the D pulse, both in amplitude and waveform morphology.

For example in receiver B, we find from ray-tracing that the D signal has undergone refraction within the deep firn, reaching a minimum depth of 85 m. The D signal pulse experiences minimal changes to its amplitude and shape between the different ice models, with the waveforms looking identical by eye. Minor amplitude shifts between the spectra are visible on the left hand plot, with a residual spectral amplitude of 10^{-2} relative to the average of the spectra. The R signal has reached a minimum depth of 3 m, and has necessarily passed through the variable shallow firn, and the changes to the amplitude and shape of the pulse are visible to the eye, along with shifts in arrival time to the order of $\mathcal{O}(\text{ns})$. The spectra also exhibit marked differences, with changes to the frequency of maximum amplitude between the RX spectra and that of the TX, as well as bumpiness. The relative residuals of the spectral amplitude are $\mathcal{O}(10^{-1})$ and higher. The changes in the spectral shape are due to the diffraction of the secondary

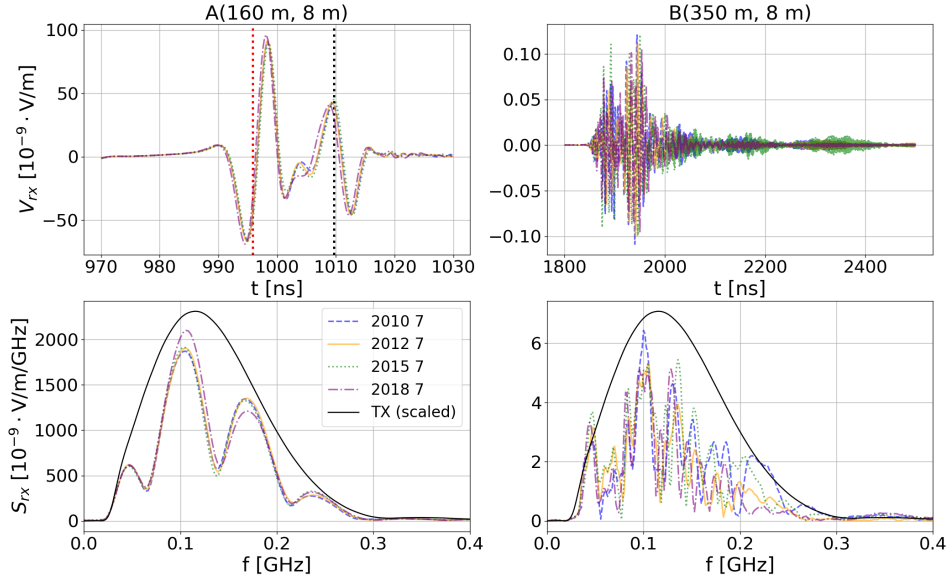


FIG. 7: Waveforms measured by a receiver at $z_{rx} = 8$ m and $x_{rx} = 160$ & 350 m. For the trace at receiver A on the left most plots ($x_{rx} = 160$), it is possible to distinguish between two wavelets, and the spectral peaks and troughs are a result of the combination of overlapping wavelets. For receiver B, the waveform is some combination of multiple wavelets that can not be isolated and identified. The RT derived arrival times of the D and R signals at Receiver A are indicated with dotted lines.

pulse as it traverses the shallow firn.

C. Spatial Variation

To quantify seasonal fluctuations in RF fluence on a year to year scale, we compare simulated outputs from July of each year between 2010 and 2020, and examine the average variation in the fluence and propagation time for the individual pulse components.

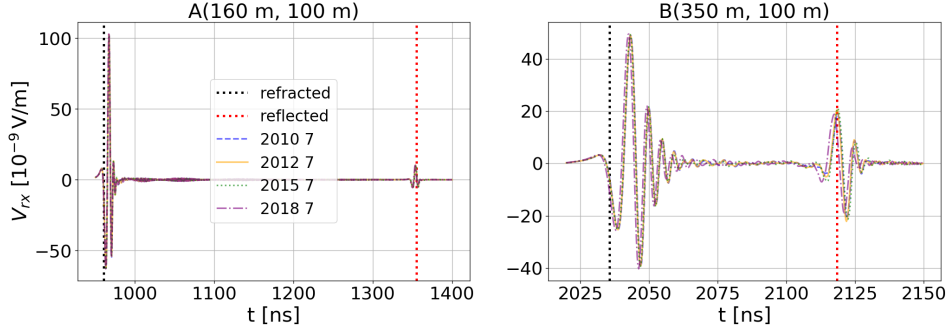
1. Fluence

The resulting spatial distributions of the fluence variation coefficient $\delta\phi^E/\phi^E$ are shown in Fig. 9, with separate heatmaps of the primary signal (Fig. 9a), and the secondary signal (Fig. 9b). In both cases the variation is lowest for deep receivers in the reflection zone, remaining below 10^{-2} . The three propagation zones stand out with distinct patterns with low variation in the reflection zone for both the primary and secondary fluence, and enhanced variation of the secondary fluence relative to the primary in the refraction zone.

Moving outward from the reflection boundary x_L , the secondary signal variation rises sharply, exceeding 10^{-1} across much of the refraction zone. The heatmaps reveal banded structures within the shallow firn that align with the fluence interference patterns of Fig. 6b. These arise from diffraction on refrozen layers, whose

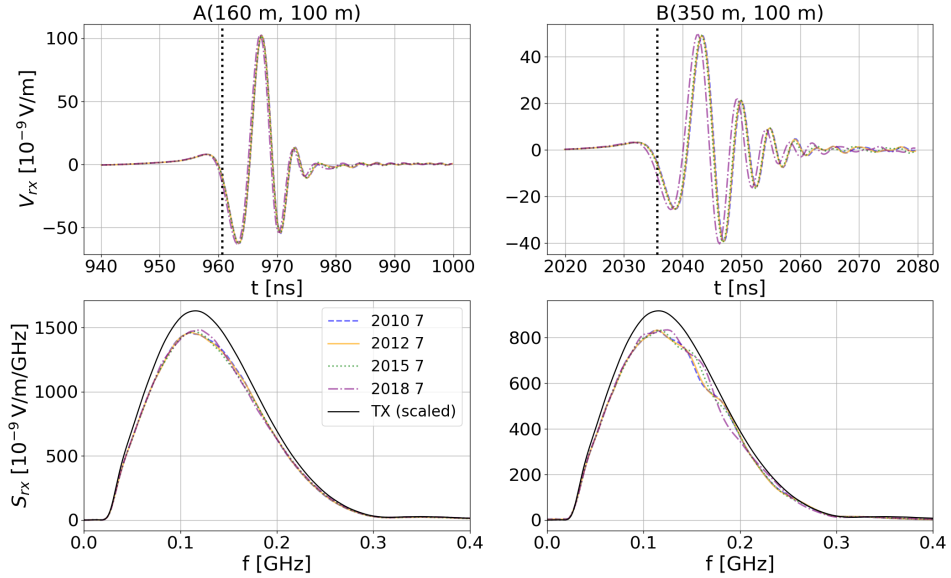
downward migration with surface accumulation causes the interference bands to shift. As a result, signals exiting the shallow refraction zone acquire range-dependent amplitudes and reach deep receivers with quasi-random strengths. Three clear bands of high variation appear between the reflection and shallow-refraction boundaries, with a fourth beginning near $z_{rx} = 160$ m. Additional hotspots occur close to the shallow refraction boundary, including a bright region with relative variation above 0.1 between ranges of 200–400 m, and generally elevated values for shallow receivers in the shadow zone. However once again, as this lies in the ‘overlap region’, these results are difficult to disentangle from the primary signal.

In contrast, the primary signal remains stable, with a variation coefficient below 10^{-2} throughout the reflection and refraction zones. Because these pulses travel mainly through deeper firn and glacial ice - where density fluctuations are small ($\Delta\rho \lesssim 1 \text{ kg/m}^3$) - their amplitudes are largely unaffected. This is illustrated in Fig. 10, which shows the distribution of relative fluence residuals to the mean at 100 m depth across receiver ranges of 160–500 m. Within the refraction zone, the secondary (reflected) signal exhibits fluctuations that are at least an order of magnitude larger than those of the primary (direct) signal, with the spread of the violin plots indicating the range of variability between years. This elevated variation reflects the greater sensitivity of the refracted/reflected paths to small changes in the firn density profile, whereas the direct path remains



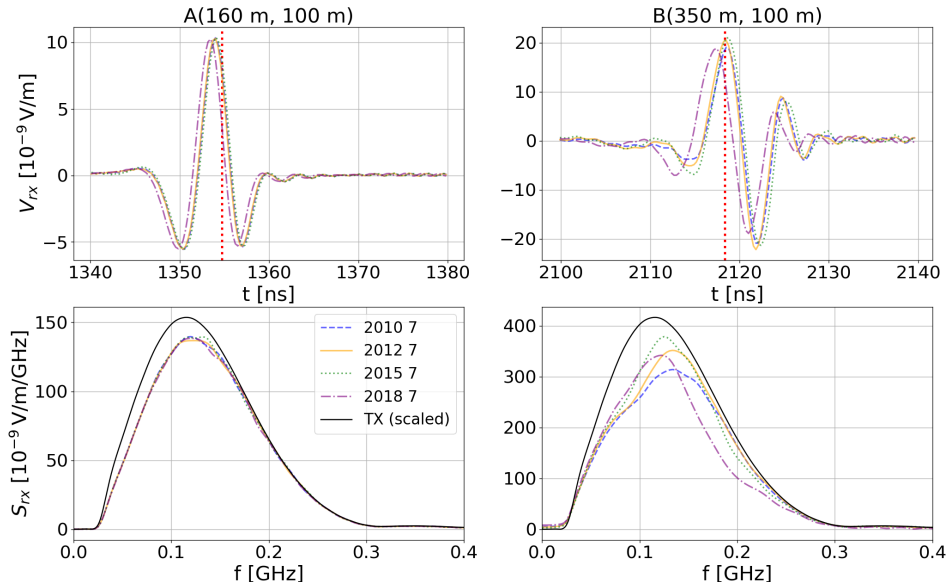
(a) Full waveform at receivers A and B (left and right respectively).

RX Primary (D) spectra



(b) Primary (D) pulses and spectra, shown in the upper and lower plots respectively.

RX Secondary (R) spectra



(c) Secondary (R) pulses and spectra, shown in the upper and lower plots respectively.

FIG. 8: Signals observed for a ‘deep’ receiver at $z_{rx} = 100$ m and $x_{rx} = 160$ & 350 m. The expected propagation times of the D and R signals from ray tracing are indicated by vertical lines in the waveform plots.

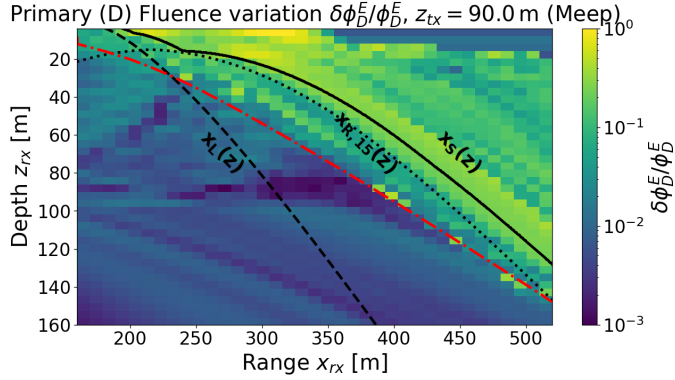
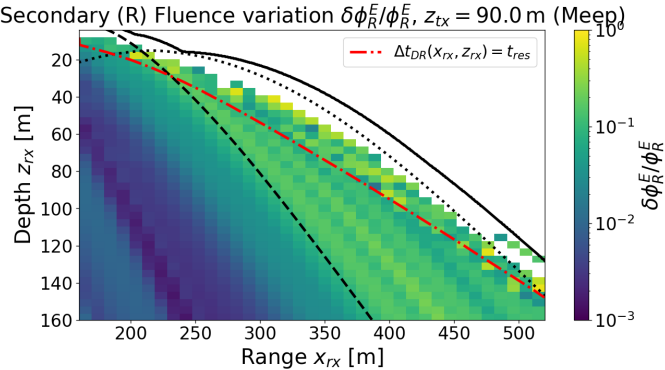
(a) D-fluence variation coefficient: $\delta\phi_D^E/\phi_D^E$ (b) R-fluence variation coefficient: $\delta\phi_R^E/\phi_R^E$

FIG. 9: Heatmaps showing the variation coefficient of the fluence $\delta\phi^E/\phi^E$ for the ice models for month 7 and years 2010 through to 2020 (a: D-fluence, b: R-fluence).

comparatively stable until approaching the caustic and shadow boundaries. Beyond the overlap boundary, the primary's signal variation rises rapidly, approaching a value similar to the shallow refracted signals, an effect likely related to interference of the direct and secondary signal. We remind the reader that beyond the shadow boundary $x > x_S$, the primary (D) signal is simply defined as the brightest peak in the waveform and may not necessarily correspond the shortest earliest arriving signal component in the waveform, a fact indicated with a change of color in the violin plot.

Fig. 11 presents the distribution of the variation coefficient of the secondary fluence $\delta\phi_R^E/\phi_R^E$ for each receiver, classified by reflection and refraction zones, and normalized to the total number of receivers (we exclude receivers that are located within the overlap zone). The reflection zone's distribution reaches its peak at $\delta\phi_R^E/\phi_R^E \approx 9.97 \cdot 10^{-3}$, corresponding to the median value of the distribution. In comparison, the refraction zone distribution peaks at the median value of $\delta\phi_R^E/\phi_R^E \approx 0.125$. The mean and median values of the respective distributions of fluence relative variation coefficient, for the direct, secondary and total waveforms,

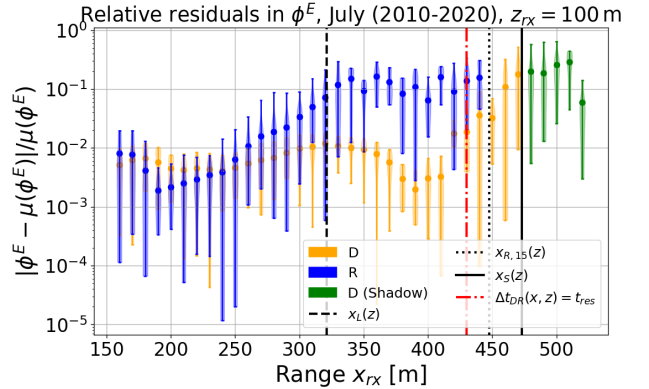


FIG. 10: The violin plots show the distribution of relative residuals in the signal fluence $|\phi^E - \mu(\phi^E)|/\mu(\phi^E)$, for the July ice models over the years 2010–2020, shown at receiver depth $z_{rx} = 100$ m. The lines indicate the boundaries between the propagation zones. Within the refraction zone, the variation in the R signal fluence exceeds that of the D signal by an order of magnitude. Within the shadow zone $x > x_L$, the definition of the primary 'D' signal is decoupled from ray-tracing.

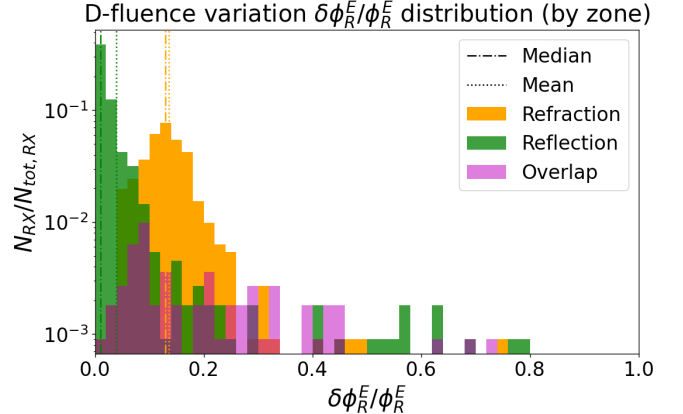


FIG. 11: The distribution of R-fluence variation coefficient $\delta\phi_R^E/\phi_R^E$ by propagation zone, with the mean and median values displayed (and summarized in Table II).

are summarized in Table II.

2. Propagation Time

We investigated variation in the propagation time of the direct (D) and secondary pulse (R) components, and by extension the relative time between them Δt_{DR} , as defined by the time of maximum amplitude for each waveform component. Here we quantify the absolute variation (or standard deviation) in the absolute propagation time t_D and the relative delay time Δt_{DR} over

Zone	Geometry	$\delta\phi_D^E/\phi_D^E [\%]$	$\delta\phi_R^E/\phi_R^E [\%]$	$\delta\phi_{\text{tot}}^E/\phi_{\text{tot}}^E [\%]$	$\delta t_D [\text{ns}]$	$\delta\Delta t_{DR} [\text{ns}]$
Reflection	$x_{rx} < x_L(z_{rx})$	0.89 (0.63)	3.86 (0.97)	0.84 (0.61)	0.19 (0.18)	0.72 (0.58)
Refraction	$x_L(z_{rx}) < x_{rx} < x_s(z_{rx})$	2.89 (0.81)	13.58 (12.91)	2.89 (2.04)	0.42 (0.30)	1.05 (0.86)
Shadow	$x_{rx} > x_s(z_{rx})$	19.43 (15.5)	-	16.63 (12.60)	9.31 (2.18)	-
Overlap	$\Delta t_{DR}(x_{rx}, z_{rx}) < t_{res}$	7.58 (5.23)	20.58 (14.32)	7.568 (5.2282)	0.53 (0.39)	1.45 (0.86)

TABLE II: The mean and median fluctuation in RF parameters in different propagation domains. For the fluence variation coefficients, the mean average is shown outside the brackets and the median is shown within the brackets.

2010–2020. As noted before within the shadow zone it's not possible to confidently identify a solitary reflected or refracted pulse, with the shadow zone waveforms appearing as a superposition of many different ray paths. Thus, we do not draw conclusions about Δt_{DR} within the shadow zone.

The spatial distribution of δt_D and $\delta\Delta t_{DR}$ are shown in the heatmaps in Fig. 12 (Fig. 12a and Fig. 12b respectively) and the variation by zone is summarized in Table II. The normalized distribution across receivers of δt_D and $\delta\Delta t_{DR}$, grouped by propagation zone, are displayed in Fig. 13 (Fig. 13a and Fig. 13b respectively). In comparison to the signal amplitude and fluence, the density fluctuations have only a minor effect on the propagation time outside the shadow zone. The distribution of δt_D within the illuminated zone is almost entirely sub-nanosecond level, with mean values of 0.19 ns and 0.42 ns for the reflection and refraction zones, respectively. By contrast, the shadow zone shows a much wider distribution extending from \approx zero to \sim 10 ns, with a mean value of 9.31 ns. However, it should be noted that our estimates of t_D correspond to the maximum amplitude time rather than the time of the shortest path from the source to the receiver within the shadow zone, complicating the interpretation of this value. Given the comparatively low amplitude of shadow zone signals, they are comparatively difficult to detect given instrumental and environmental noise. In Appendix D, we also examine the variation of t_D using an alternative identification method, based on the time that the cumulative amplitude rises above a threshold. We found that this alternative definition of arrival time results in a lower degree of seasonal variation as compared to the maximum-amplitude definition.

The distribution of the relative time variations $\delta\Delta t_{DR}$ for the reflection and refraction zones includes the increased fluctuations in the path and time of the secondary signals relative to the primary, with mean values of 0.72 ns and 1.05 ns respectively. These fluctuations are well below the \sim 20 ns width of the pulses. In contrast to t_D , these fluctuations are directly observable for a single receiver. While we also display the variation of $\delta\Delta t_{DR}$ within the shadow zone for completeness, the physical interpretation of the estimated Δt_{DR} in the shadow zone is unclear for reasons already stated.

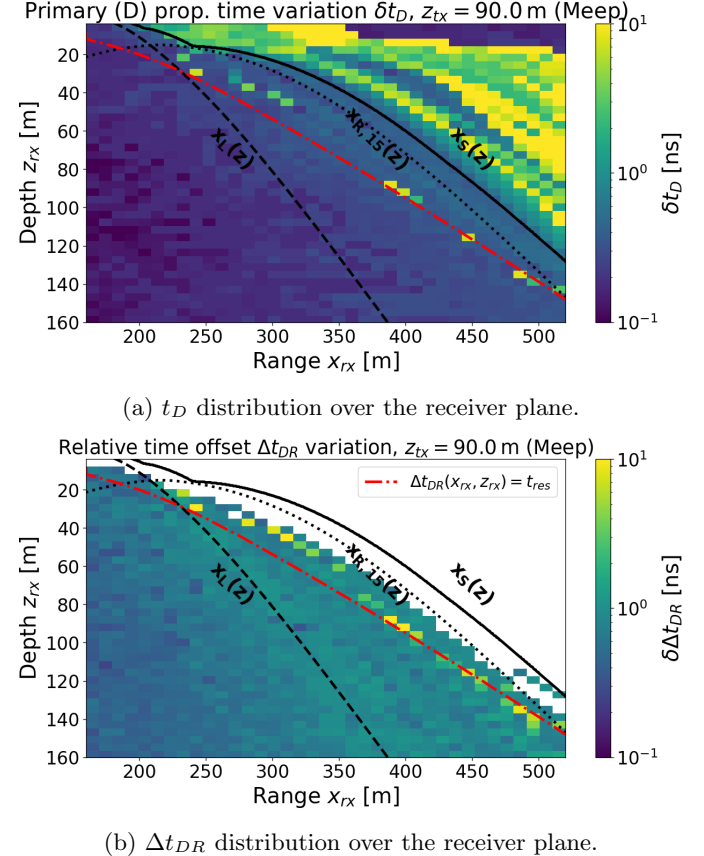


FIG. 12: Heatmap of the absolute variation of the direct propagation time t_D relative time delay Δt_{DR} at a transmitter at $z_{tx} = 90.0 \text{ m}$. Overlaid ray trajectories $x_L(z)$, $x_{R,15}(z)$, and $x_S(z)$ mark the boundaries between the reflected, refracted and shadowed regions, while the an additional line in red indicates the threshold beyond which $\Delta t_{DR} < t_{res} = 12.82 \text{ ns}$.

In a ray optics picture, the magnitude of Δt_{DR} fluctuations within the illuminated zones, 0.1 ns to 1.8 ns, appears to correspond to propagation path changes on the order of $\mathcal{O}(10 \text{ cm})$, accumulated on propagation paths $\mathcal{O}(100 \text{ m})$ from the source to the receivers – seasonal perturbations in the density profile can yield subtle changes in propagation path. The direct pulse propagates along a relatively stable, refracted path, while the secondary pulse interacts more strongly with

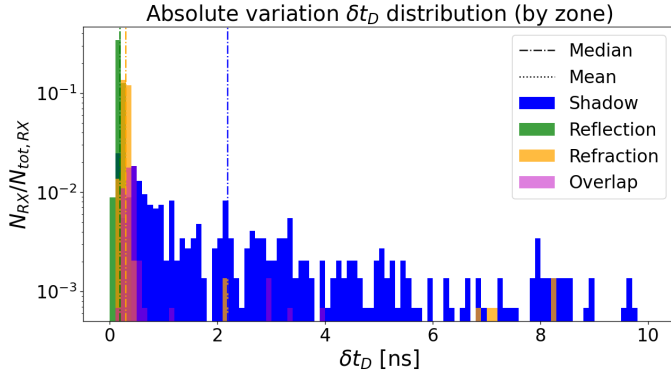
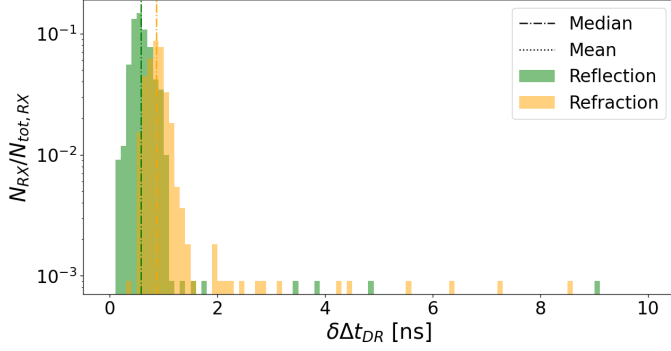
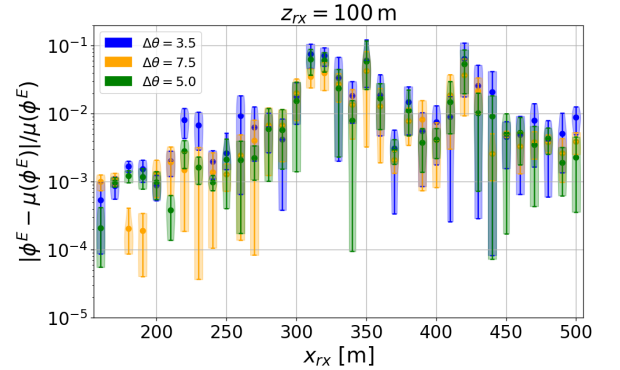
(a) distribution by propagation zone δt_D Absolute variation $\delta\Delta t_{DR}$ distribution (by zone)(b) Δt_{DR} distribution by propagation zone

FIG. 13: Normalized distribution by of the absolute variation in t_D (top) and Δt_{DR} (bottom) by propagation zone; reflection, refraction and shadow.

over-dense layers, grazing near-critical angles where small seasonal variations in $n(z)$ can induce larger relative shifts. This difference leads to the observed 0.1–1.8 ns scatter in most of the illuminated domain, with localized enhancements along the shadow boundary. Nonetheless, while these values are small compared to the overall pulse width they are potentially observable in radio neutrino detectors.

D. Bandwidth dependence

Since the magnitude and spectral width of an Askaryan pulse is dependent on the observer angle relative to the Cherenkov angle, and given that the fluence fluctuations we have discussed are a product of inter-layer diffraction, we investigated the dependence of the fluence variation of shallow refracted signals on the bandwidth of the original signal. To accomplish this, we repeated the RF simulation procedure with two source signals of successively wider bandwidth, corresponding to a Cherenkov angle offset of $\Delta\theta = 3.5^\circ$ & $\Delta\theta = 5.0^\circ$ in addition to the $\Delta\theta = 7.5^\circ$ signal used thus far. The resulting pulses were both brighter and

FIG. 14: $\delta\phi^E/\phi^E$ for different bandwidth signals

had greater spectral width and narrower time-width, with their properties summarized in Table I and their spectra shown in Fig. 5. Because of the limitations of the FDTD method for higher frequencies at this scale, we utilize the PE method to simulate the pulses across the same domain used for the FDTD simulations.

The variation coefficient of the total pulse fluence $\delta\phi_{tot}^E/\phi_{tot}^E$ for the different input signal bandwidths is shown for a receiver at a depth of 100 m in Fig. 14, showing that the magnitude of the signal variation indeed increases for larger bandwidth signals. This is further evidence that the fluctuations in fluence are a result of the self-interference of signals traversing the shallow firn. Higher bandwidth pulses are sensitive to smaller length scales of the refractive index, and hence are subject to higher degrees of variability.

E. Zenith dependence

From the point of view of an in-ice radio neutrino observatory, the dependence of the amplitude and fluence variation on the path taken through the firn is useful, as it means that for a given receiver depth, there exists a volume of the ice for which the aforementioned signal variation is expected when the neutrino vertex is located within this zone. Assuming a cylindrical fiducial volume with a depth of 2700 m and radius 3000 m and receiver at $z_{rx} = 100$ m, approximately 18.5% of the volume would be located in the receiver's shallow refraction zone, such that ray tracing predicts a path from an observable neutrino-induced radio signal to the receiver that undergoes refraction within the shallow firn without undergoing reflection. This corresponds to $\approx 22\%$ of the illuminated (non-shadowed) volume.

In principle, one can use the RF arrival angle at the receiver to discriminate which neutrino events are subject to these effects. If the neutrino vertex is deeper than the receiver depth $z_{rx} = 100$ m, rays arriving at a zenith angle of $\theta_{zen} < 46^\circ$ will have undergone reflection

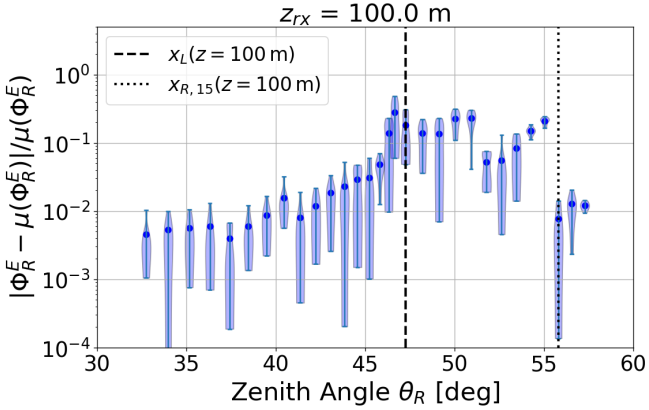


FIG. 15: Variation of fluence for $z_{rx} = 100$ m as a function of zenith angle θ_R .

off the surface, rays arriving between $46^\circ < \theta_R < 56^\circ$ will have undergone refraction in the shallow firn, while rays $56^\circ < \theta_R < 90^\circ$ underwent refraction between z_{550} and the receiver depth, with all other rays below these angles arriving directly from the neutrino vertex. The dependence of the fluence variation with zenith angle can be seen in Fig. 15, with events with a mean $\delta\phi_R^E/\phi_R^E > 10^{-2}$ arriving within a range of zenith angles $40^\circ < \theta_R < 55^\circ$, and a narrower region $48^\circ < \theta_R < 55^\circ$ constraining events with $\delta\phi_R^E/\phi_R^E > 10^{-1}$.

V. IMPLICATIONS FOR NEUTRINO DETECTORS

The RF simulations discussed in Section IV suggest that for a significant fraction of neutrino events, $> 18\%$, seasonal firn fluctuations will result in relative uncertainty of > 0.1 for the power of the secondary signal (reflecting/refracting) for a receiver antenna located at depths utilized by past and current in-ice Askaryan detectors.

Furthermore, this effect appears to be frequency-dependent, as evidenced by the increase in variation for higher bandwidth source pulses seen in Fig. 14. The properties of interest in neutrino physics and astronomy are the primary neutrino's energy E_ν , flavor and arrival direction $(\varphi_\nu, \theta_\nu)$ (with φ being the azimuthal direction and θ the polar direction). Together these may indicate the location of the neutrino sources, the nature of these sources, and the nature of ultra-high energy cosmic rays, for example, from mass composition measurements at the highest energies. Additionally, it has been shown that the neutrino-nucleon cross-section can be constrained to within a factor of 2 of the Standard Model cross-section above 10 PeV with only 10 neutrino events for a generic detector with 1 degree angular resolution and one decade of energy resolution [7]. An understanding of seasonal effects is thus im-

portant to eventual measurements of neutrino properties.

The accuracy of neutrino energy, vertex and arrival direction reconstruction is contingent on the ability to reconstruct radio emission properties at the source given the available information at the detector. This includes the location of the source of the radio emission (which is in close proximity to the interaction vertex), the radiation pattern, and the total emitted energy. These can in principle be discerned from the RF signal amplitude, arrival direction, polarization, and spectral content. Given the lack of an established method for determining neutrino flavor from RF emission, in this Section we estimate the approximate uncertainty in neutrino energy and arrival direction resulting from the seasonal variation in RF fluence within the illuminated zone. We assume perfect reconstruction of the electric field $E(RX, t)$ at the receiver RX from the received voltage $V(RX, t)$, neglecting detector-specific antenna effects. Since the PE simulation explicitly assumes a vertically polarized signal under cylindrical symmetry and the FDTD code used in this study makes the same assumption, our current simulations are unable to comment on seasonal influences on polarization reconstruction; that topic is deferred for future work.

To demonstrate the seasonal variation in the reconstructed neutrino parameters, we model a string of 6 vertically polarized antennas in a phased array between depths of $z_{rx,min} = 96$ m to $z_{rx,max} = 120$ m, spaced at 4 m intervals, located at some range $x_{rx,ph}$ from the source and within the illuminated zone. The vertex position (x_{tx}, z_{tx}) is calculated by finding an optimal fit to the arrival times of the MEEP-simulated waveforms at the receivers using ray tracing, described in greater detail below in Section V A. A signal arrival direction θ_{RX} and signal propagation distances L are then estimated for the direct and secondary signals arriving at an equivalent antenna located in the center of the phased array, and the uncertainty is found from the variation in the parameters across the ice models. The spectrum-derived quantities - i.e., the viewing angle offset $\Delta\theta_{VC}$, fluence ϕ^E and ultimately shower energy E_{sh} for the phased array - are calculated from the coherent average of the D and R waveform components at each antenna in the array, with the coherent averages estimated independently for each component, and the variation in the resulting averaged waveform as described in Section V B. Additionally, we address the impact of seasonal variation on neutrino reconstruction within the shadow zone in the Appendix D.

A. Vertex Reconstruction

Given a model of the ice, when the phased array is within the illuminated zone, the source position may be inferred via ray tracing. The accuracy of the reconstruc-

tion is dependent on the accuracy of the ice model as well as the experimental timing resolution. Consequently, the seasonal variation in the arrival times discussed in Section IV C 2 impose a limit on the resolution of the source reconstruction. As we approximated the neutrino source with a dipole source, all rays arriving at the receiver are convergent on the position of the source at $(x_{tx} = 0, z_{tx} = 90 \text{ m})$.

Utilizing the `radioprop` numerical ray-tracer implemented in the NuRadioMC module `SignalProp`, we calculate an array of arrival times t_D^{RT} and t_R^{RT} for an array of transmitting antennas located within depths, $10 \text{ m} < z_{tx} < 200 \text{ m}$, ranges $-100 \text{ m} < x_{tx} < 100 \text{ m}$, with spacings of $\Delta z_{tx} = 2 \text{ m}$ in depth and $\Delta x_{tx} = 10 \text{ m}$. The ray tracing solutions were estimated using a double-exponential profile (quantified by Eq. 1) fit to the CFM profile $n_{CFM,2010,1}(z)$, with the fit parameters described in the Appendix E. The rays are sampled at receiver antennas with depths corresponding to the aforementioned phased array and located at ranges $150 \text{ m} < x_{rx} < 500 \text{ m}$ with spacing $\Delta x_{rx} = 20 \text{ m}$. For each point in this array, we use MEEP to estimate a penalty score χ^2 from the offset of the arrival times estimated of the D and R signals from ray-tracing, relative to the time of the first arriving direct signal at the highest receiver $t_0 = t_D(z_{rx,min})$. The penalty score for $\Delta t_D = t_D - t_0$ is then:

$$\chi_D^2(x_{tx}, z_{tx}, x_{rx}) = \sum_i^{N_{ph}} |\Delta t_D^{RT}(x_{tx}, z_{tx}, x_{rx}, z_{rx,i}) - \Delta t_D^{mEEP}(x_{rx}, z_{rx,i})|^2, \quad (4)$$

Where N_{ph} is the number of antennas in the phased array and i corresponds to the number of the phased array channel, indexed from $z_{rx,min}$ to $z_{rx,max}$. The best fit source $(x_{tx,reco}, z_{tx,reco})$ is therefore found from the minimum penalty score. The penalty score χ_R^2 is estimated similarly for t_R , which is still offset from the earliest arrival time $t_0 = t_D(z_{rx,min})$. Finally, a combined penalty score χ_{DR}^2 is estimated by multiplying the two: $\chi_{DR}^2 = \chi_D^2 \cdot \chi_R^2$. We estimate the penalty scores across the ensemble of sources and receivers, for each ice model $n_{CFM}(z)$ utilized in the Results Section IV, and thereby estimate the variation in the reconstructed source position. We include an example of penalty scores χ^2 mapped over the candidate TX space, as well as a plot of reconstructed TX positions in Appendix E.

By taking the best-fit source position, we can further estimate the variation in propagation lengths L_D & L_R from the source to average depth of the receiver string $\hat{z}_{rx} = (z_{rx,min} + z_{rx,max})/2$. In the same way, we also estimate launch $\theta_{TX,D}$ & $\theta_{TX,R}$ and receiver angles $\theta_{RX,D}$ & $\theta_{RX,R}$ at the average receiver depth. Since variations in the launch angles and receiver angles exhibit absolute correlation, it is sufficient for our

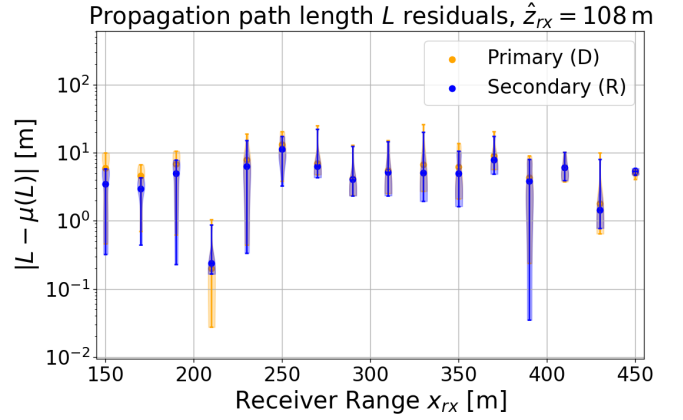


FIG. 16: Propagation length L reconstruction.

purposes to consider the variation in the receiver angle alone. The variation in the reconstructed propagation path length L , both for the direct path and the secondary path are shown as a function of range x_{rx} in Fig. 16. In comparison to variation in the fluence, the variation in the propagation path is relatively flat, with a change $1 \text{ m} \lesssim \delta L \lesssim 10 \text{ m}$ across the receiver range until the shadow zone, with minimal difference between D and R signal components. This property follows from the vertex reconstruction being estimated from the propagation time, and the relatively minor difference in the variation of arrival times within the reflection and refraction zones. The change in the propagation time appears to be a function of the vertical path taken by the ray between the source and the receiver. A similar picture emerges for the derived receiver angle, as outlined in Section V C. The residual errors in the path length additionally contribute to the energy uncertainty, albeit as a sub-leading uncertainty as outlined in the following Section.

B. Energy Reconstruction

Reconstructing energy from a received Askaryan signal is challenging due to the dependence of the observed spectrum on the offset angle $\Delta\theta_{VC}$ between the observer (or, alternatively, viewing angle θ_V with respect to the Cherenkov angle θ_C). As $\Delta\theta_{VC}$ increases, the overall signal strength diminishes, and the spectral bandwidth also diminishes as shorter wavelengths lose coherence faster than longer wavelengths. For illustration, we can suppose that we observe a single pulse (direct, reflected or refracted) originating from the neutrino vertex, and we measure the fluence ϕ^E . The square root of the fluence is directly proportional to the deposited shower energy $\sqrt{\phi^E} \propto E_{sh} = E_\nu \cdot \kappa$, where E_ν is the primary neutrino's energy and κ is the fraction of the primary's energy that goes into the shower. For purely hadronic showers, κ is equal to the neutrino inelasticity y , however if the inter-

action is charged current and results in a lepton depositing energy into the observed shower, then $\kappa > y$. Additionally, the fluence diminishes with the propagation distance L of the wavefront due to geometric spreading and attenuation losses, described with a path loss function $h(L) = \exp(-L/L_\alpha)/L$. The fluence of a single-component Askaryan pulse is expressed then as [56]:

$$\sqrt{\phi^E} \propto E_{sh} \cdot h(L) \cdot f(\Delta\theta_{VC}), \quad (5)$$

where $f(\Delta\theta_{VC})$ parametrizes the root of the fluence with respect to the viewing angle offset. If we consider a two-component (D & R) signal, each wavefront will have propagated over distances L_D and L_R and have different spectra corresponding to different effective viewing angles θ_{V_D} and θ_{V_R} ; correspondingly, we express ϕ^E as the sum of ϕ_D^E and ϕ_R^E :

$$\begin{aligned} \phi^E &= \phi_D^E + \phi_R^E \\ \phi_D^E &\propto [E_{sh} \cdot h(L_D) \cdot f(\Delta\theta_{VC_D})]^2 \\ \phi_R^E &\propto [E_{sh} \cdot h(L_R) \cdot f(\Delta\theta_{VC_R})]^2. \end{aligned} \quad (6)$$

Consequently, the uncertainty in shower energy estimation is a function of the uncertainties in the measured fluence as well as the reconstructed viewing angle of each signal component and the reconstructed propagation distances. It is clear from inspection that for a single component signal the relative uncertainty in fluence $\delta\phi^E/\phi^E$ is linearly proportional to that of the relative energy uncertainty:

$$\frac{\delta E_{sh}}{E_{sh}} \propto \frac{1}{2} \frac{\delta\phi^E}{\phi^E}. \quad (7)$$

Given the frequency dependence of coherent radio emission, the shape of the frequency spectrum can be used as a proxy for the viewing angle. An established technique is to quantify the frequency spectrum using a slope parameter s [56], which is the ratio of the integrated fluence for two distinct bands, with frequency limits f_0 & f_1 , and f_1 & f_2 , respectively:

$$s = \frac{\phi_{f_0, f_1}^E}{\phi_{f_1, f_2}^E}, \quad (8)$$

such that generally, the slope parameter will grow larger as the viewing angle offset increases, as the high frequency band diminishes in power relative to the lower band. As an example, we adopt the band limits of $f_0 = 130\text{ MHz}$, $f_1 = 200\text{ MHz}$ & $f_2 = 300\text{ MHz}$, and the parameterization of the shower energy [56]:

$$E_{sh} \propto \sqrt{\phi_{130, 300}^E} \cdot g(s), \quad (9)$$

Where $g(s)$ is:

$$g(s) = \frac{1}{p_2(\ln s)^2 + p_1 \ln s + p_0}, \quad (10)$$

and p_2 , p_1 and p_0 are parameters derived from simulation. In the case of the source spectrum corresponding to $\Delta\theta_{VC} = 7.5^\circ$ the values $p_0 = 6.46$, $p_1 = -16$ & $p_2 = 12.45$ are used [56]. The relative uncertainty in shower energy is therefore a linear combination of the relative uncertainties in the root of the lower band fluence $\sqrt{\phi_{f_0, f_1}^E}$, the slope parameter function $g(s)$, and in the path loss function $h(L)$. While $h(L)$ is an independent parameter, there is obvious correlation and covariance between s and ϕ_{f_1, f_2}^E . To derive the uncertainty for a given phased array observation, we divide the waveforms at each receiver into the primary (D) and secondary (R) components. The coherent average of each waveform component is then taken independently, and the slope parameter and fluence estimated from the resulting spectrum for the equivalent central antenna at \hat{z}_{rx} . Combining the spectrum-derived quantities with the variation in the path length, we then estimate the variation in the reconstructed energy $\delta E_{sh}/E_{sh}$ across the ice models. The relative variation in each of the spectrum-derived quantities and the spread loss are shown in Fig. 17, and the derived result for the shower energy in Fig. 18. It is seen that, for the secondary signal, the variation in the slope parameter is the dominant contribution to the energy uncertainty, with the shape and magnitude $\mathcal{O}(10^{-1})$ of the variation matching closely between the slope parameter and shower energy and the largest variations occurring in the refraction zone as expected. The path length loss is a sub-leading source of variability for the secondary signal, however it forms a relatively flat floor for the shower-energy variation for the direct signal $\delta E_{sh}/E_{sh} \sim \mathcal{O}(10^{-2})$.

C. Arrival Direction

Again taking the case of a single component Askaryan pulse measured at a given receiver, the reconstruction of the primary neutrino's arrival direction $(\varphi_\nu, \theta_\nu)$ requires measurement of the arrival direction of the wavefront $(\varphi_{RX}, \theta_{RX})$, the aforementioned viewing angle offset from the Cherenkov angle $\Delta\theta_{VC}$, and the polarization angle α_p [57], with the latter being the argument of the ratio of the vertical E_θ and horizontal E_ϕ components of the field (as defined the convention defined in [58]):

$$\alpha_p = \arctan\left(\frac{E_\theta}{E_\phi}\right). \quad (11)$$

The uncertainty in the neutrino arrival direction will be a linear combination of the uncertainties of the receiver arrival direction, the polarization angle and the viewing angle offset from the Cherenkov angle, as these values are independent of one another. We comment on the polarization reconstruction in Section V D.

From the vertex reconstruction exercise in Section V A, we can estimate the variation in the receiver arrival

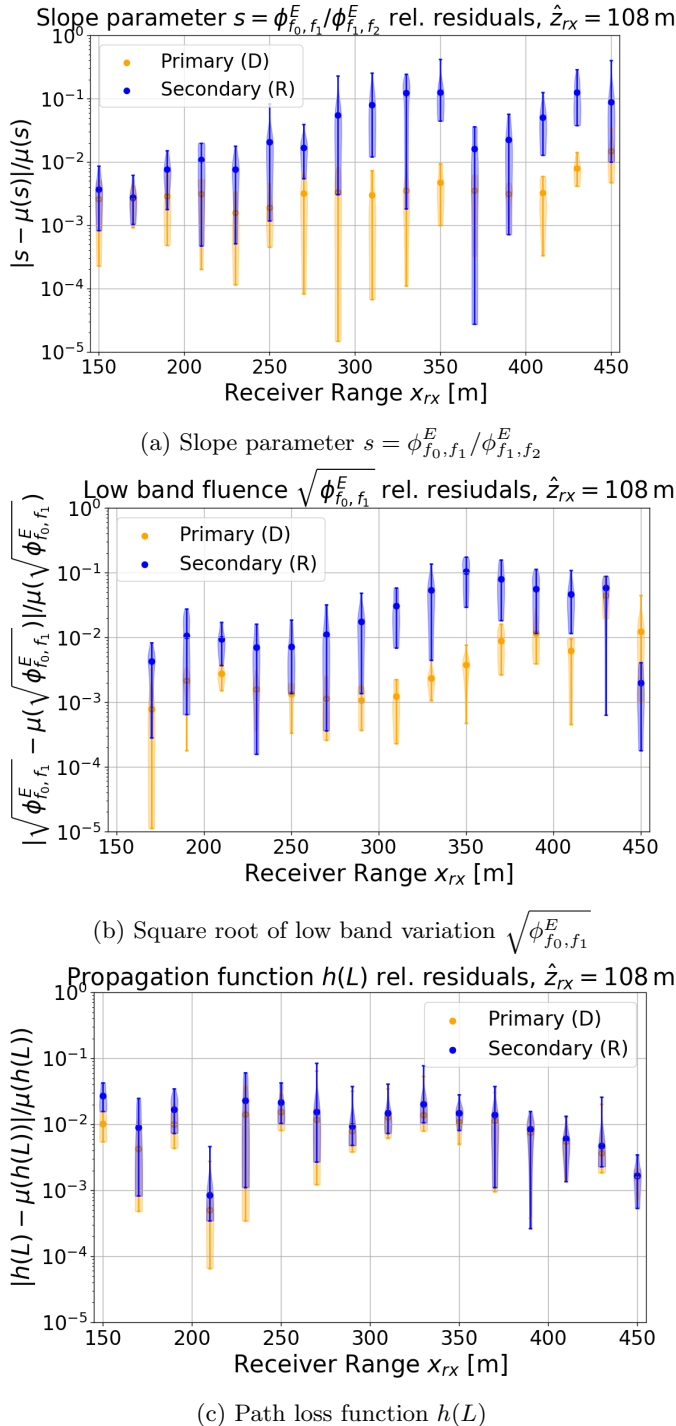


FIG. 17: Relative variation in the spectrum-derived parameters: the slope parameter s , the square root of the low-band fluence $\sqrt{\phi_{f_0, f_1}^E}$, and the path loss function $h(L)$

direction $\theta_{RX,D}$ and $\theta_{RX,R}$ from the variation in the reconstructed source position (x_{tx}, z_{tx}) . The results found by minimizing χ_{DR}^2 are displayed as a function of range x_{rx} in Fig. 19a. To obtain the residual error

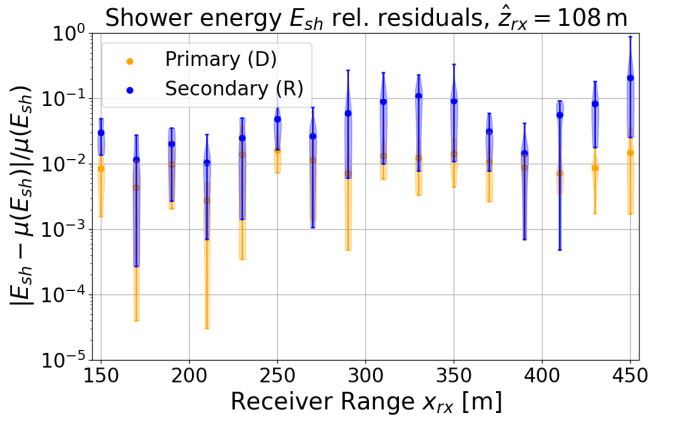


FIG. 18: Relative variation in the reconstructed shower energy E_{sh}

$\Delta\theta_{VC}$, we take the variation in the slope parameter s from Section V B and, by exploiting the linear proportionality between $\log(s)$ and $\Delta\theta_{VC}$, obtain the variation as a function of range as shown in Fig 19b. The total uncertainty in the polar angle component of the neutrino arrival direction is shown in Fig. 19c. The variation in the receiver angle, derived from vertex reconstruction, is relatively flat across the spatial range of 150 m to 400 m, but is an order of magnitude greater for the secondary signal $0.1^\circ \lesssim \delta\theta_{RX,R} \lesssim 1^\circ$ as compared to the primary signal $\delta\theta_{RX,D} \lesssim 0.1^\circ$. It also forms the leading source of error for the derived neutrino angle variation. The viewing angle offset uncertainty is greater for the secondary signal and is largest within the refraction zone, as expected from our observations of the spectrum, and is generally an order of magnitude lower than the uncertainty for the receiver arrival angle. Overall, the magnitude and shape of the neutrino angle variation as a function of range is effectively identical to that of the receiver arrival angle, and we can expect variations on the order of $\delta\theta_{\nu,R} \sim 0.5^\circ$ when considering the secondary signal alone and $\delta\theta_{\nu,D} \sim 0.05^\circ$ when considering the direct signal alone.

D. Polarization

Previous works have noted that the relatively large systematic errors in the polarization angle reconstruction $\delta\alpha_p \sim \mathcal{O}(10^\circ)$ are typically the dominant source of uncertainty in neutrino arrival-direction reconstruction for deep in-ice receiver arrays [57]. Whereas shallow arrays have achieved polarization angle resolutions of $\delta\alpha_p \sim 1.3^\circ$ [59], the lower gain, cross-polarization isolation, and signal-to-noise ratio of deep-borehole Hpol antennas makes it difficult to accurately reconstruct the horizontally polarized field E_ϕ from the measured voltage trace [57].

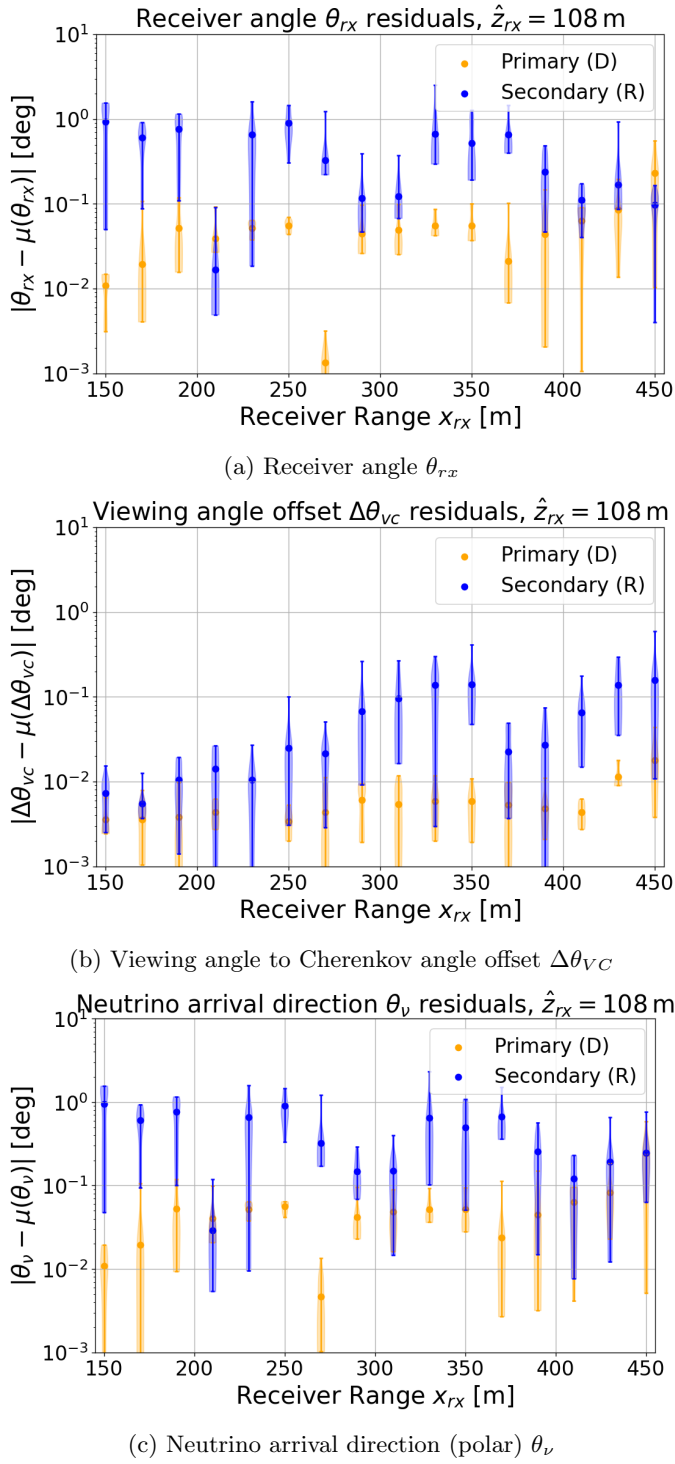


FIG. 19: Variation in the receiver arrival angle θ_{rx} , the viewing angle to Cherenkov angle offset $\Delta\theta_{VC}$ and the neutrino polar arrival direction θ_ν .

By construction, the PE method used by `paraProp` can not estimate E_ϕ as it is derived for a cylindrically symmetric medium. This symmetry was also utilized in the FDTD simulations using `MEEP`. The limitations of

the simulations and consequent neglect of birefringence effects meant that we could not make meaningful statements about the influence of seasonal ice variation on the horizontally polarized field E_ϕ , nor on resulting errors in the polarization and azimuth angle reconstruction. Given that the aforementioned α_p uncertainty exceeds our estimates of neutrino zenith angle variation θ_ν by at least an order of magnitude, a dedicated study of seasonal ice variation on E_ϕ may be warranted, but would require a different modeling approach than that used in this study and must explicitly incorporate birefringence into the ice model.

VI. CONCLUSION

We have found that in-ice radio neutrino detectors are sensitive to seasonal changes in the density of the upper firn layer, particularly the formation of refrozen ice layers, which lead to fluctuations in refracted and reflected signals on the order of $\delta\phi_R^E/\phi_R^E \gtrsim \mathcal{O}(10^{-1})$ for signals arriving with zenith angles in the range $45^\circ < \theta_{RX} < 55^\circ$. Although this study has focused on detectors searching for Askaryan emission, similar variations in signal fluence and arrival time are expected for radar signals traversing the shallow firn. The implications for parameter reconstruction in future radar echo detectors, however, will differ and depend strongly on the depths spanned by the detector, and are therefore beyond the scope of this work.

For an Askaryan detector with a fiducial volume of 2700 m depth and 3000 m radius, approximately 18% of UHE neutrino event vertices are expected to produce shallow refracted events that must pass through the shallow firn, a fraction that rises to 22% if one excludes the shadow zone from the volume. In addition, secondary signals observed in both the reflection and refraction zones exhibit arrival-time variations on the scale of $\mathcal{O}(0.1\text{--}1.8\text{ ns})$. The primary consequence for event reconstruction is a systematic uncertainty in the reconstructed shower energy E_{sh} for events with both observable primary and secondary signals, at the level of $0.01 \lesssim \delta E_{sh}/E_{sh} \lesssim 0.1$, with the magnitude of the uncertainty depending on the relative strengths of the direct and secondary signals. Stronger fluctuations at higher frequencies ($f > 250$ MHz) may also introduce uncertainty in the estimation of the viewing-angle offset from the Cherenkov angle, $\Delta\theta_{VC}$. Background variations in signal arrival times further limit vertex reconstruction resolution and, consequently, the estimated arrival direction and propagation length. We find arrival-direction uncertainties of $\delta\theta_{RX,R} \sim \mathcal{O}(0.1^\circ\text{--}0.5^\circ)$ for refracted signals and $\delta\theta_{RX,D} \sim \mathcal{O}(0.05^\circ)$ for direct signals, which, in the absence of an up-to-date ice model, represent a small but irreducible systematic uncertainty. It is worth commenting that the estimates of energy and arrival direction variation are done under optimistic assumptions of perfect field reconstruction, the detection

and identification of both D and R signal components, and are done in the absence of noise.

Variations in signal fluence and time of flight within the refraction zone appear stochastic, while correlating with the presence of refrozen layers along the ray path. This suggests that *in-situ* ice measurements at a given detector site, combined with forward glaciological modeling of snow accumulation and temperature, may allow for the construction of an up-to-date ice model that enables identification of the shallow refractive propagation zone relative to receiver arrays. It is not clear whether the detailed amplitude and timing fluctuations within this zone can be fully mitigated through modeling, particularly given uncertainties in receiver positioning within the ice and horizontal variation in the firn.

Finally, variations in signal fluence may reduce antenna multiplicity and thereby degrade reconstruction

quality. Detector-specific analyses are therefore required to fully quantify reconstruction systematics. The influence of firn density anomalies on polarization-angle reconstruction was not examined in this study, but certainly merits further investigation. As polar temperatures continue to warm in both the Arctic and Antarctic, density and temperature anomalies in the firn are expected to become increasingly important considerations for neutrino event reconstruction.

ACKNOWLEDGMENTS

We sincerely thank our colleagues in the RET collaboration for their comments, particularly I. Esteban, I. Loudon, J. Ralston and K. de Vries. We recognize support from the National Science Foundation under grant numbers 2306424, 2019597 and 2012989, as well as from the John D. and Catherine T. MacArthur Foundation.

[1] V. S. Berezinsky and G. T. Zatsepin, in *International Cosmic Ray Conference*, International Cosmic Ray Conference, Vol. 1 (1970) p. 55.

[2] M. Ahlers and F. Halzen, *Physical Review D* **86**, 10.1103/physrevd.86.083010 (2012).

[3] K. Kotera and A. V. Olinto, *Annual Review of Astronomy and Astrophysics* **49**, 119–153 (2011).

[4] G. T. Zatsepin and V. A. Kuz'min, *Soviet Journal of Experimental and Theoretical Physics Letters* **4**, 78 (1966).

[5] K. Greisen, *Phys. Rev. Lett.* **16**, 748 (1966).

[6] S. Aiello *et al.* (KM3NeT), *Nature* **638**, 376 (2025), [Erratum: *Nature* 640, E3 (2025)].

[7] I. Esteban, S. Prohira, and J. F. Beacom, *Physical Review D* **106**, 10.1103/physrevd.106.023021 (2022).

[8] M. S. Muzio, *The European Physical Journal Special Topics* 10.1140/epjs/s11734-025-01502-5 (2025).

[9] R. Abbasi, M. Ackermann, J. Adams, *et al.* (IceCube Collaboration), *Phys. Rev. Lett.* **135**, 031001 (2025).

[10] K. Kotera, D. Allard, and A. Olinto, *Journal of Cosmology and Astroparticle Physics* **2010** (10), 013–013.

[11] M. Aartsen, M. Ackermann, J. Adams, *et al.*, *Physical Review D* **98**, 10.1103/physrevd.98.062003 (2018).

[12] G. A. Askar'yan, *Zh. Eksp. Teor. Fiz.* **41**, 616 (1961).

[13] J. A. Aguilar, P. Allison, D. Besson, *et al.*, arXiv e-prints , arXiv:2212.10285 (2022), arXiv:2212.10285 [physics.ins-det].

[14] S. Barwick, D. Besson, P. Gorham, and D. Saltzberg, *Journal of Glaciology* **51**, 231–238 (2005).

[15] C. Allen, A. Bean, D. Besson, *et al.*, *New Astronomy Reviews* **42**, 319 (1998).

[16] A. Anker, S. Barwick, H. Bernhoff, *et al.*, *Advances in Space Research* **64**, 2595–2609 (2019).

[17] P. Allison, J. Auffenberg, R. Bard, *et al.*, Design and initial performance of the askaryan radio array prototype eev neutrino detector at the south pole (2011), arXiv:1105.2854 [astro-ph.IM].

[18] J. Aguilar, P. Allison, and J. Beatty, *Journal of Instrumentation* **16** (03), P03025.

[19] C. Deaconu, L. Batten, P. Allison, *et al.*, *Journal of Cosmology and Astroparticle Physics* **2021** (04), 017.

[20] Q. Abarr, P. Allison, J. Ammerman Yebra, J. Alvarez-Muñiz, *et al.*, *Journal of Instrumentation* **16** (08), P08035.

[21] A. Anker, S. Barwick, H. Bernhoff, *et al.*, *Journal of Cosmology and Astroparticle Physics* **2020** (03), 053–053.

[22] I. Kravchenko, G. Frichter, T. Miller, *et al.*, *Astroparticle Physics* **20**, 195 (2003).

[23] P. Allison, S. Archambault, J. Beatty, *et al.*, *Physical Review D* **102**, 10.1103/physrevd.102.043021 (2020).

[24] S. Hoover, J. Nam, P. W. Gorham, *et al.*, *Phys. Rev. Lett.* **105**, 151101 (2010).

[25] C. Glaser, *EPJ Web of Conferences* **216**, 02008 (2019).

[26] S. Agarwal, J. A. Aguilar, N. Alden, and et al., arXiv e-prints , arXiv:2512.17664 (2025), arXiv:2512.17664 [astro-ph.HE].

[27] S. Prohira, K. de Vries, P. Allison, *et al.*, *Physical Review Letters* **124**, 10.1103/physrevlett.124.091101 (2020).

[28] S. Prohira, K. de Vries, P. Allison, *et al.*, *Physical Review D* **104**, 10.1103/physrevd.104.102006 (2021).

[29] P. Allison, J. Beatty, D. Besson, *et al.*, Initial performance of the radar echo telescope for cosmic rays, ret-cr (2024), arXiv:2409.07511 [hep-ex].

[30] C. Buizert and M. Helsen, in *Glaciers and Ice Sheets in the Climate System. Springer Textbooks in Earth Sciences, Geography and Environment*, edited by A. Fowler and F. Ng (Springer, Cham, 2020) Chap. 11, pp. 255–277.

[31] V. Verjans, A. A. Leeson, M. McMillan, and et al., *Geophysical Research Letters* **48**, e2020GL092060 (2021), e2020GL092060 2020GL092060.

[32] J. A. Aguilar, P. Allison, D. Besson, *et al.*, Precision measurement of the index of refraction of deep glacial ice at radio frequencies at summit station, greenland (2023), arXiv:2304.06181 [astro-ph.IM].

[33] M. W. Hörhold, S. Kipfstuhl, F. Wilhelms, *et al.*, *Journal of Geophysical Research: Earth Surface* **116** (2011).

[34] H. Jay Zwally and L. Jun, *Journal of Glaciology* **48**, 199–207 (2002).

[35] I. M. Howat, *Journal of Glaciology* **68**, 1076–1084 (2022).

[36] NOAA Global Monitoring Laboratory, Summit, greenland [sum], <https://gml.noaa.gov/dv/site/SUM.html> (2025), accessed: 2025-12-19.

[37] J. R. Blackford, *Journal of Physics D: Applied Physics* **40**, R355 (2007).

[38] A. Kyriacou, PoS **ICRC2025**, 313 (2025).

[39] R. L. Hawley, E. M. Morris, and J. R. McConnell, *Journal of Glaciology* **54**, 839–845 (2008).

[40] R. Alley and B. Koci, *Annals of Glaciology* **10**, 1–4 (1988).

[41] S. Ali, P. Allison, S. Archambault, *et al.*, Modeling the refractive index profile $n(z)$ of polar ice for ultra-high energy neutrino experiments (2024), arXiv:2406.00857 [astro-ph.IM].

[42] M. M. Herron and C. C. Langway, *Journal of Glaciology* **25**, 373–385 (1980).

[43] C. M. Stevens, V. Verjans, and J. e. a. Lundin, *Geoscientific Model Development* **13**, 4355 (2020).

[44] A. L. Giese and R. L. Hawley, *Journal of Glaciology* **61**, 503–510 (2015).

[45] R. L. Hawley, *Borehole Investigations of Firn Processes*, Ph.D. thesis, University of Washington (2005).

[46] Global modeling and assimilation office (gmao) (2015).

[47] P. Kuipers Munneke, S. Ligtenberg, B. Noël, I. Howat, J. Box, E. Mosley-Thompson, J. McConnell, K. Steffen, J. Harper, S. Das, *et al.*, *The Cryosphere* **9**, 2009 (2015).

[48] A. Kovacs, A. J. Gow, and R. M. Morey, *Cold Regions Science and Technology* **23**, 245 (1995).

[49] A. F. Oskooi, D. Roundy, M. Ibanescu, P. Bermel, J. Joannopoulos, and S. G. Johnson, *Computer Physics Communications* **181**, 687 (2010).

[50] S. Prohira, C. Sbrocco, A. P., and et al., *Physical Review D* **103**, 10.1103/physrevd.103.103007 (2021).

[51] C. Glaser *et al.*, *Eur. Phys. J. C* **80**, 77 (2020), arXiv:1906.01670 [astro-ph.IM].

[52] T. Winchen, in *European Physical Journal Web of Conferences*, European Physical Journal Web of Conferences, Vol. 216 (EDP, 2019) p. 03002, arXiv:1810.01780 [astro-ph.IM].

[53] J. Alvarez-Muñiz, W. R. Carvalho, M. Tueros, and E. Zas, *Astroparticle Physics* **35**, 287–299 (2012).

[54] J. Alvarez-Muñiz, R. A. Vázquez, and E. Zas, *Physical Review D* **62**, 10.1103/physrevd.62.063001 (2000).

[55] C. Deaconu, A. Vieregg, S. Wissel, J. Bowen, S. Chipman, A. Gupta, C. Miki, R. Nichol, and D. Saltzberg, *Physical Review D* **98**, 10.1103/physrevd.98.043010 (2018).

[56] J. A. Aguilar, P. Allison, J. J. Beatty, *et al.*, *The European Physical Journal C* **82**, 10.1140/epjc/s10052-022-10034-4 (2022).

[57] I. Plaisier, S. Bouma, and A. Nelles, *The European Physical Journal C* **83**, 10.1140/epjc/s10052-023-11604-w (2023).

[58] A. Connolly, *Phys. Rev. D* **105**, 123012 (2022).

[59] A. Anker, P. Baldi, S. Barwick, and et al., *Journal of Cosmology and Astroparticle Physics* **2022** (04), 022.

[60] J. Alvarez-Muñiz and E. Zas, *Physics Letters B* **411**, 218 (1997).

[61] A. Kovacs, A. J. Gow, and R. M. Morey, A reassessment of the in-situ dielectric constant of polar firn (1993).

[62] H. Bader, *Journal of Glaciology* **2**, 319–323 (1954).

[63] C. Glaser, Neutrino direction and energy resolution of askaryan detectors (2019), arXiv:1911.02093 [astro-ph.IM].

[64] A. Anker, S. Barwick, H. Bernhoff, *et al.*, *Journal of Cosmology and Astroparticle Physics* **2019** (11), 030.

[65] Mark v ice coring system.

[66] R. J. Arthern, D. G. Vaughan, A. M. Rankin, R. Mulvaney, and E. R. Thomas, *Journal of Geophysical Research: Earth Surface* **115** (2010).

[67] R. V. Buniy and J. P. Ralston, *Physical Review D* **65**, 10.1103/physrevd.65.016003 (2001).

[68] GISP2 Stake Field / Climate Data, Annual snow accumulation at summit, greenland, <https://climatechange.umaine.edu/gisp2/data/accum.html> (2025), accessed: 2025-12-19.

[69] D. Besson, *European Physical Journal Special Topics* **234**, 4985 (2025).

[70] Equipment comparison – nsf ice drilling progra, <https://icedrill.org/equipment/comparison>, accessed: 6 February 2026.

Appendix A: Firn Densification

After initial drifting, packing, and disintegration of the snow crystals, fallen snow has a density of approximately $\rho_s \approx 0.3 \text{ g/cm}^3$, forming a mixture of approximately two-thirds air to one-third ice. Compaction and grain growth dominate the densification process until the firn density reaches $\rho \sim 0.55 \text{ g/cm}^3$, from which point the densification rate slows and sintering becomes the dominant process [30]. Sintering involves distinct ice grains gradually bonding to form an interconnected but porous ice matrix, as mass transport across grain surfaces and through the vapor phase increases the contact area between grains and reduces pore space [30, 37]. At $\rho = 0.73 \text{ g/cm}^3$, the densification rate again slows as the area of contact between ice grains reaches a maximum, and the remaining air occupies thin channels within the grain boundaries [30]. The density continues to increase due to internal deformation or creep of crystals. The final densification stage is the ‘bubble close off’, beginning at $\rho = 0.8 – 0.84 \text{ g/cm}^3$, where the overburden pressure causes the remaining bubbles of air to shrink until their pressure matches that of the surrounding ice.

The benchmark densification model was derived by Herron-Langway using depth-density data from 17 firn cores [42]. The HL model postulates that a change in pore space at a given depth is linear in the change in stress due to the weight of the newly accumulated snow, and assumes Sorge’s Law: the vertical velocity of the material dz/dt is equal to the accumulation rate A divided by ρ [62]. It is, therefore, possible to derive a simple differential equation model describing the density change with depth and with time:

$$\frac{d\rho}{dz} = k\rho(\rho_i - \rho) \quad \text{and} \quad \frac{d\rho}{dt} = kA(\rho_i - \rho), \quad (\text{A1})$$

from which one can simply derive an asymptotic exponential function for the density profile:

$$\rho(z) = \rho_i + (\rho_s - \rho_i)e^{-kz}. \quad (\text{A2})$$

The HL-model additionally describes the densification rate k as having an Arrhenius dependence on temperature, with an inflection point at $z = 0.55 \text{ g/cm}^3$ accounting for the transition from grain growth to sintering:

$$\begin{aligned} \frac{d\rho}{dt} &= k_0 A^{1.0}(\rho_i - \rho), k_0 = 11 \cdot e^{-\frac{Q_0}{RT}}, \text{ if } \rho \leq 0.55 \text{ g/cm}^3 \\ \frac{d\rho}{dt} &= k_1 A^{0.5}(\rho_i - \rho), k_1 = 575 \cdot e^{-\frac{Q_1}{RT}}, \text{ if } \rho > 0.55 \text{ g/cm}^3, \end{aligned} \quad (\text{A3})$$

With the activation energies Q_0 and Q_1 determining the sensitivity of k to temperature. The majority of firn densification models utilize the same assumptions as the HL model, albeit with moderately different formulations of k_0 and k_1 .

Numerous empirical and theoretical models exist for relating ρ to the relative permittivity (or dielectric constant) ϵ_r and hence refractive index $n = \sqrt{\epsilon_r}$. One of the most commonly used is a simple linear relationship derived from measurements at the McMurdo Ice Shelf [48]:

$$n(z) = n_0 + B\rho(z). \quad (\text{A4})$$

The constant term n_0 is usually set to $n_0 = 1$ to correspond to the refractive index of the vacuum, but this is not universal in the literature[48, 61]. Various estimates of $B = 0.840 - 0.851 \text{ cm}^3/\text{g}$ exist in the literature, with $B = 0.845 \text{ cm}^3/\text{g}$ being the most frequently cited[48, 61].

Appendix B: Community Firn Model

We relied upon the Community Firn Model glaciological simulation framework to generate realistic ice models for the RF simulations presented in section IV [43]. Here we give a more detailed overview of the glaciological modeling workflow, including the starting and boundary conditions and the climatological data used for the forcing of the firn.

CFM modeling occurs in two stages. The first is a “spin-up” stage that establishes a self-consistent initial density profile for the model. The spin-up begins with the analytic Herron-Langway solution for firn density, computed using the long-term mean accumulation rate and temperature at Summit Station; this profile serves as a smooth initial guess. The model then evolves forward in time using the chosen densification equation. At each step, new layers are added at the surface and old layers removed from the base until the entire grid has been “flushed” and replaced by model-generated layers. This

ensures that the profile reflects both the densification physics and the climatological forcing, rather than the arbitrary analytic starting guess. After spin-up, the ‘main run’ begins, using the full time-varying climate forcing from January 1980 to December 2021. During both spin-up and main runs, the model evolves density, temperature, and age for each firn layer, and can additionally track grain size, isotopes, and meltwater where relevant.

1. Input Data

The input data used to drive the CFM simulation is derived from the Modern-Era Retrospective analysis for Research and Application (version 2) dataset or MERRA-2 [46]. MERRA-2 is a global atmospheric reanalysis produced by NASA’s Global Modeling and Assimilation Office, spanning from 1980 to the present. It combines a wide range of satellite and in-situ observations with a numerical weather prediction model to generate a continuous, physically consistent record of atmospheric and surface climate. In the dataset, the Earth is divided into a grid with each cell having resolution 0.5° in latitude by 0.66° longitude. MERRA-2 provides surface air temperature, precipitation, accumulation rate, and other fields at monthly resolution, which we use as boundary conditions to force the evolution of the firn density profile. In Fig. 20 we show the monthly input data for the mass accumulation rate A (Fig. 20a), the skin temperature T_{skin} (Fig. 20b), as well as the melting events which are quantified by the volume of surface melt water per unit area V_{melt} (Fig. 20c).

Appendix C: Modeling Askaryan radiation

Simulating the full first-principles radio emission of a neutrino-induced particle cascade is highly challenging due to the complexity of the underlying reactions. Radio Cherenkov emission or *Askaryan* radiation is the result of a build-up of a net negative charge excess in a relativistic cascade propagating through a dense medium with a speed of $v > c/n$. The excess negative charge builds up as positrons are annihilated while Compton and δ -electrons from the surrounding medium join the shower [12]. The resulting time-varying charge distribution radiates electromagnetic waves, which combine coherently at wavelengths comparable to the longitudinal shower scale a (typically $a \sim \mathcal{O}(0.1 \text{ m})$ in ice) near the Cherenkov angle θ_C .

For observers at viewing angles θ_V displaced from θ_C , coherence is progressively lost; shorter wavelengths de-cohere more rapidly than longer wavelengths, and the overall signal strength falls sharply for $|\theta_V - \theta_C| \gtrsim 2.4^\circ$ for hadronic showers. Thus, the observed Askaryan spectrum is strongly dependent on the viewing angle

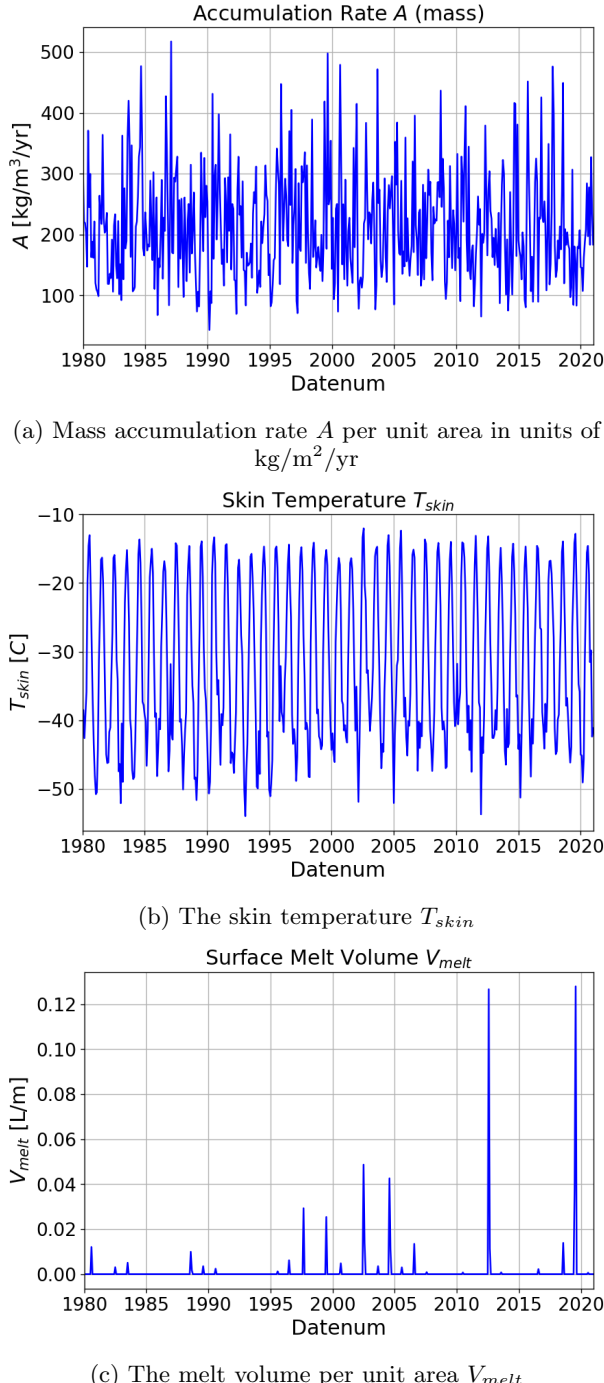


FIG. 20: A time series of the monthly climate data (1980-2021) from MERRA-2 used to drive the evolution of the firm in CFM. From top to bottom: the mass accumulation rate A , skin temperature T_{skin} and melting volume per unit area V_{melt} .

offset $\Delta\theta_{VC}$.

To specify the frequency dependence of the injected pulse in our simulations, we adopted the widely used

Alvarez-Muñiz & Zas (AMZ) parameterization of the Askaryan electric field spectrum [54]. In this model, the spectral amplitude is expressed as a function of the shower energy E_{sh} , frequency f and viewing angle θ_V :

$$\frac{E(E_{sh}, f, \theta_V)}{[\text{V}/\text{m}/\text{MHz}]} = 2.53 \cdot 10^{-7} \frac{E_{sh}}{[\text{TeV}]} \frac{f}{f_0} \frac{1}{1 + (\frac{f}{f_0})^{1.44}} g(E_{sh}, f, \theta_V), \quad (\text{C1})$$

with a characteristic frequency scale $f_0 = 1.15 \text{ GHz}$. The angular factor $g(f, \theta_v)$:

$$g(E_{sh}, f, \theta_v) = \frac{\sin(\theta_v - \theta_c)}{\sin(\theta_c)} \exp(-\ln 2 \cdot [\frac{\theta_v - \theta_c}{\sigma_\theta(E_{sh}, f)}]^2), \quad (\text{C2})$$

encodes the off-cone suppression and the narrowing of the coherent bandwidth as a function of frequency. The angular width $\sigma_\theta(E_{sh}, f)$ depends on the shower type (hadronic or electromagnetic) and energy; electromagnetic showers become elongated at high energies due to the Landau-Pomeranchuk-Migdal (LPM) effect[53, 60]. An example of the resulting waveform and spectrum was shown in Fig 5. The expected narrowing of the spectrum and rapid suppression of amplitude for increasing θ_V are clearly visible.

It is important to note that the AMZ parametrization is used here purely as a convenient spectral form factor for defining the reference test pulse in the simulations. We do not rely on it as a complete or strictly causal model of Askaryan emission, nor do we attempt to model the near-field structure of a real hadronic shower at $E_{sh} > 10^{16} \text{ eV}$. More rigorous and causal treatments of Askaryan radiation exist, i.e. Buniy & Ralston [67], but utilizing these does not change the conclusions of this work, which depend on the relative changes in fluence and timing induced by seasonal changes in the ice structure.

Appendix D: Neutrino reconstruction in the Shadow Zone

Our discussion of event reconstruction in section V has assumed unambiguous detection of the D and R pulses along a phased array of Vpol antennas within the illuminated zone. In the shadow zone, this condition is not satisfied and it is exceedingly difficult, if not impossible, to estimate the true vertex position via ray-tracing. As a consequence, the propagation distance L from the receiver to the source is ambiguous, with an uncertainty in the distance on the scale of the attenuation length $\delta L \sim \mathcal{O}(L_\alpha) \sim \mathcal{O}(\text{km})$, leading to $\delta g(L)$ dominating the shower energy uncertainty, which would span multiple energy-decades.

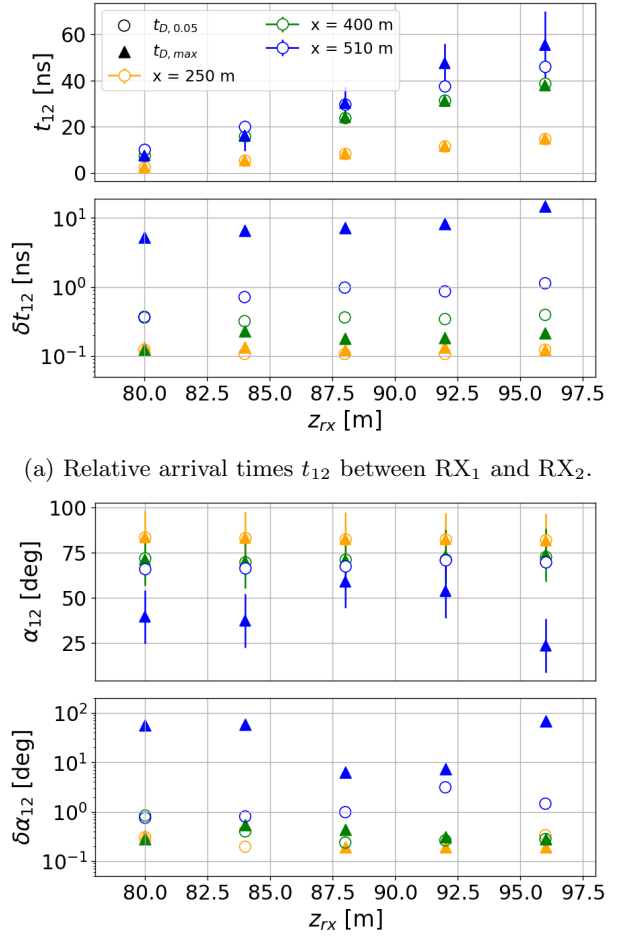
To address the situation for arrival direction, we

make the crude approximation that the rays have propagated in a straight line from the source to a pair of receivers at $z_{rx} > 80$ m within the shadow zone. Under this assumption, we estimate the angle α_{12} of this straight line path with respect to the horizontal between antennas RX_1 and RX_2 :

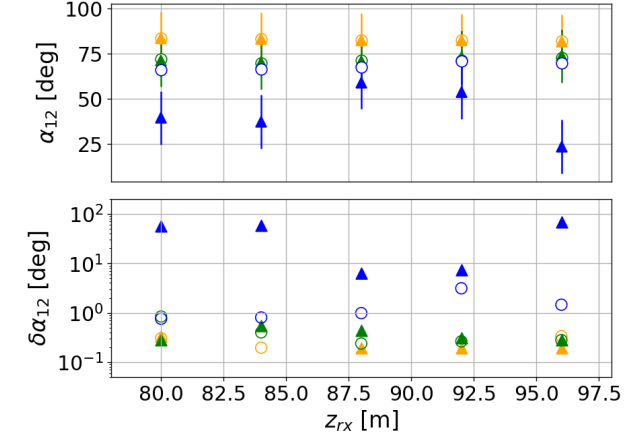
$$\tan(\alpha_{12}) = \frac{n(z_{\text{mid}})\Delta z_{12}}{c\Delta t_{12}}, \quad (\text{D1})$$

where $z_{\text{mid}} = (z_{rx,1} + z_{rx,2})/2$, Δz_{12} is the depth interval between the antennas and $\Delta t_{12} = t_{D,2} - t_{D,1}$ is the relative arrival time of the waveforms at RX_1 and RX_2 . We can define t_D in two ways. The first is the ‘leading edge time’ $t_{D,0.05}$, which we quantify here as the time at which the cumulative amplitude of the waveform reaches 5% of the sum total. The second is the time of maximum amplitude of the waveform $t_{D,\text{max}}$. The shadow waveforms displayed in Fig. 7 are a combination of complex multi-path propagation and mutual interference between different waveforms. This would suggest that $t_{D,0.05}$ would be more likely to correspond to the ‘earliest arriving’ signal. On the other hand, $t_{D,\text{max}}$ is likely to be easier to identify in a real-world detection where environmental and system noise must be considered. In this study we do not include noise in the waveforms and thus the leading edge is easier to identify than in real world conditions. As shown in Section IV C 2, the propagation time variation within the shadow zone, using $t_{D,\text{max}}$, was on a scale $\delta t \sim \mathcal{O}(10\text{ ns})$, which would imply RX arrival direction uncertainty $\delta\theta_{RX} \gtrsim \mathcal{O}(10^\circ)$, over an order of magnitude greater than within the illuminated zone. To better quantify this, we take an array of 6 receivers (RX) located at depths $76 \text{ m} \leq z_{rx} \leq 96 \text{ m}$, and for RX from $z_{rx} = 80$ m downwards, we calculate t_{12} between the RX and its neighbor using both $t_{D,0.05}$ and $t_{D,\text{max}}$, which, equivalently, allows us to calculate α_{12} . We then find the variation among the estimated values of t_{12} and α_{12} .

In Fig. 21, we plot t_{12} (21a) and α_{12} (21b) and their variations as a function of depth, where the range to the receiver array is $x_{rx} = 250$ m (reflection zone), $x_{rx} = 400$ m (refraction zone) and $x_{rx} = 510$ m (shadow zone). For the reflection and refraction zone examples, the variation in the time offset between RX pairs is $\delta t_{12} < 1\text{ ns}$, and the variation in the arrival angle at the pair is close to $\delta\alpha_{12} \sim 0.1^\circ$, consistent with our results in the previous Section. With a clearly identifiable direct pulse, there is little difference between the results when using $t_D = t_{D,\text{max}}$ and $t_D = t_{D,0.05}$. By contrast, the choice of $t_{D,\text{max}}$ and $t_{D,0.05}$ has a significant effect on both the variation in t_{12} and α_{12} . For $t_D = t_{D,0.05}$, we find variation in the arrival times on the scale of a nanosecond $\delta t_{12} \sim 1\text{ ns}$ and hence in arrival angle of $\delta\alpha_{12} \sim 1^\circ$. For $t_D = t_{D,\text{max}}$ both variations are increased by an order of magnitude or greater, with the worst-case example of $\delta\alpha_{12} \approx 67^\circ$ for $z_{rx} = 96$ m. In addition, the mean value of α_{12} differs



(a) Relative arrival times t_{12} between RX_1 and RX_2 .



(b) Arrival angle α_{12} between RX_1 and RX_2 .

FIG. 21: Relative arrival time t_{12} (21a) and inferred arrival angle α_{12} (21b) between neighboring receiver pairs as a function of receiver depth z_{rx} . Results are shown for receiver arrays at $x_{rx} = 250$ m (reflection zone), $x_{rx} = 400$ m (refraction zone), and $x_{rx} = 510$ m (shadow zone). In the top panel of each subplot the points indicate mean values across ice models, with error bars showing the standard deviation, using both the leading-edge time $t_{D,0.05}$ and the time of maximum amplitude $t_{D,\text{max}}$. The bottom panels directly plot the variation in the respective quantities among the ice models.

by 10 to 20 degrees between the two t_D methods. In this example, we find that the variation in receiver arrival direction, using receiver pairs, is on the scale of $0.8^\circ \lesssim \delta\alpha_{12} \lesssim 3^\circ$ for the leading-edge time estimate, compared to $6^\circ \lesssim \delta\alpha_{12} \lesssim 70^\circ$ using the maximum time method.

Appendix E: Illustration of transmitter source reconstruction

The Figures presented here provide supplementary visualization of the vertex reconstruction method outlined in section V A. We calculated penalty scores as a function of transmitter (TX) position for the primary and secondary signals using the `RadioPropa` ray tracer in `NuRadioMC` and the `MEEP` simulated waveforms for each ice model. The ice model used for the ray tracing solution was found using a split-exponential profile $n_{nuMC}(z)$. From the linear relationship between $n(z)$ and $\rho(z)$ (expressed with Eq. 2) [48], we can derive an expression equivalent to Eq. 1:

$$n(z) = \begin{cases} n_i + (n_s - n_i)e^{-k_0 z} & \text{if } z \leq z_{550} \\ n_i + (n_{550} - n_i)e^{-k_1(z - z_{550})} & \text{if } z > z_{550}. \end{cases} \quad (\text{E1})$$

From inspection, the exponent factors k_0 and k_1 are the same for Eq. 1 and Eq. E1. The parameters were obtained from a best fit to the CFM model corresponding to January 2010, and are as follows:

- $n_0 = 1.302$ ($\rho_0 = 0.355 \text{ g/cm}^3$),
- $k_0 = 0.025 \text{ m}^{-1}$,
- $k_1 = 0.019 \text{ m}^{-1}$,
- $z_{550} = 16.48 \text{ m}$.

The two profiles and their offsets from each other are compared in Fig. 22. For each trial position (x_{tx}, z_{tx}) , we computed χ_D^2 , χ_R^2 for primary and secondary signals respectively, and the combined score χ_{DR}^2 , as defined in Equation 4, and identified the optimal TX position from the minimum of χ_{DR}^2 . The optimal TX position then corresponds to an optimal propagation path L and signal arrival direction at the RX for the D and R signals, respectively. The TX position is estimated independently for the different ice models used to simulate the waveforms, and the variation in TX between these models translated naturally into the seasonal variation in L and θ_{RX} as shown in Sections V A and V C, respectively.

In Fig. 23a we show the penalty score map calculated for a phased array located at $x_{rx,ph} = 250 \text{ m}$ and the refractive index model $n_{2010,6}^{CFM}(z)$, with the scores for the primary χ_D^2 and secondary pulses shown in the top and middle subplots, and the combined score shown in the lower subplot. The χ_D^2 and χ_R^2 maps each show a strip of low amplitudes (low penalty scores) for various values of range; this strip corresponds to positions where a ray propagating from the source to the receiver arrive at similar angles and are launched at similar angles. Since the penalty score is calculated from the relative arrival times at the phased array, they are naturally sensitive to the angle of the wavefront with respect to the simulated phased array. The difference in

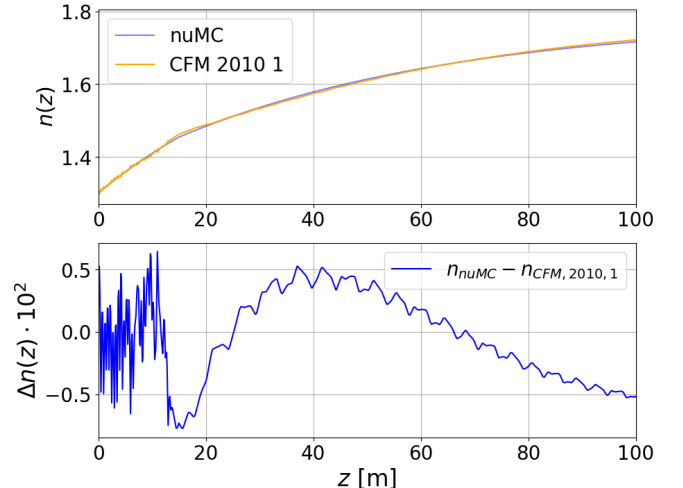


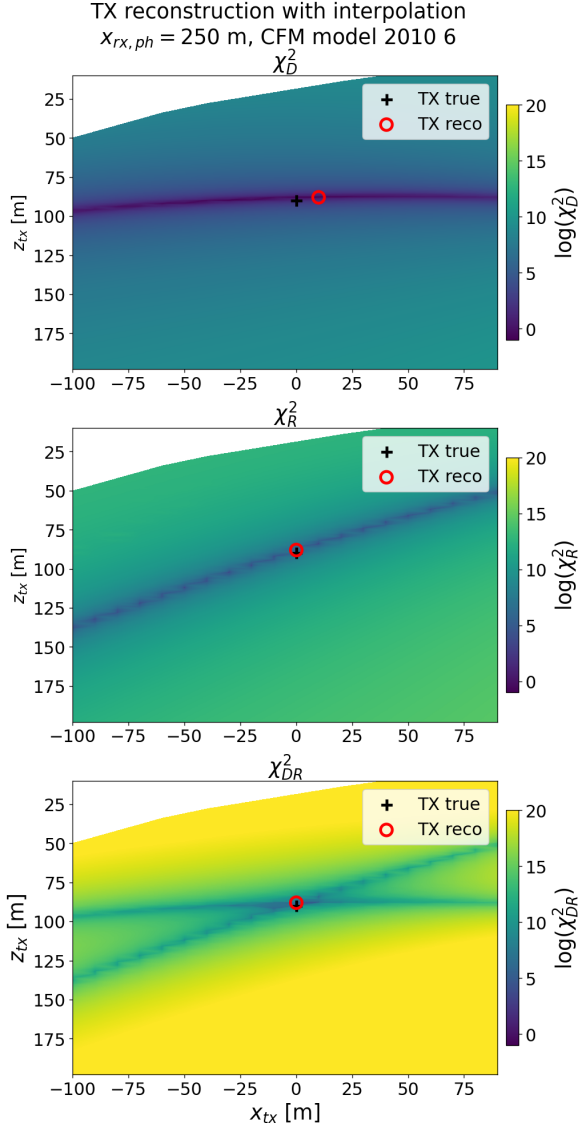
FIG. 22: The refractive index profile $n_{nuMC}(z)$ used to generate ray tracing solutions for the TX reconstruction. Top $n_{nuMC}(z)$ shown alongside a CFM profile $n_{CFM,2010,1}(z)$ corresponding to the model estimated for January 2010. The offset between the two profiles is shown in the bottom plot.

arrival angles for the primary and secondary (reflected or refracted) signals leads to the bands being inclined with respect to one another, and their product creates a cross-like shape in the χ_{DR}^2 map, whose crossing point aligns with the minimum χ_{DR}^2 value.

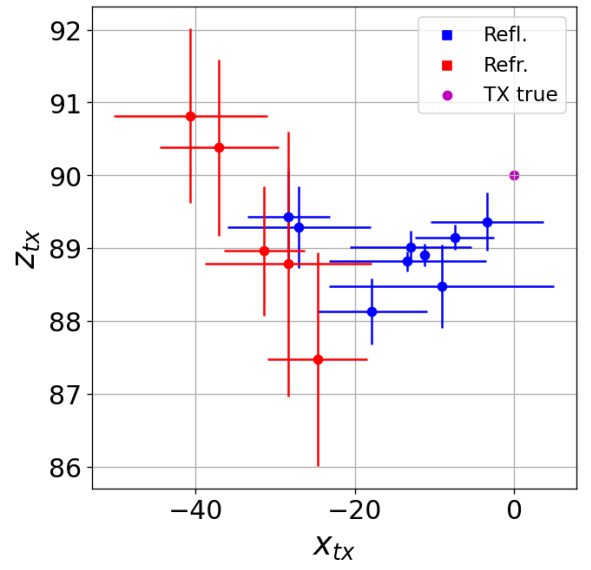
In Fig. 23b, we show the best-fit TX positions calculated for phased arrays at different ranges, with the variation between the ice models indicated with error-bars; the central point shows the mean TX position among the ice models and the error-bars represent the standard deviation over the ice models. Here, we can associate a systematic error with the systematic offset between the refractive index model used to generate the ray tracing solutions, for all of the CFM ice models used in this study. This manifests as the offset between the mean TX reconstruction values and the true TX. These are distinct from the variation between the ice models illustrated with the error-bars. The systematic offset in range in particular is due to the offset $\Delta n = n_{nuMC}(z) - n_{CFM}(z)$ of the `NuRadioMC` model relative to the CFM models. This causes an increase in the absolute delay time of the ray arriving at the receivers, and an increase in the delay relative to the first arriving signal, leading to an overestimate in the distance to the source that increases as the phased array moves down-range.

The model to model variation was generally larger for the reconstructed range as compared to the depth, and this held true for when the phased array was located in the reflection zone and refraction zones. For the range direction, this variation was $\frac{\delta x_{tx,rec}}{x_{tx,rec}} \approx 8 \text{ m}$ in

both zones, whereas the depth variation was larger in the refraction zone $\frac{\delta z_{tx,rec0}}{z_{tx,rec0}} \approx 1.35$ m compared to the reflection zone $\frac{\delta z_{tx,rec0}}{z_{tx,rec0}} \approx 0.4$ m. The systematic offset of the vertex reconstruction is generally larger than the seasonal variation, with offsets in range increasing from $x_{tx,rec0} - x_{tx,true} \approx -5$ m at $x_{rx,ph} = 160$ m to $x_{tx,rec0} - x_{tx,true} \approx -30$ m at $x_{rx,ph} = 320$ m. Within the refraction zone, the offset in the depth direction varied in both directions relative to the $z_{tx,true}$ to an extent of 87 m $\lesssim |z_{tx,rec0} - z_{tx,true}| \lesssim 91$ m, slightly larger than that for the reflection zone 88 m $\lesssim |z_{tx,rec0} - z_{tx,true}| \lesssim 89$ m.



(a) Maps of the penalty score χ^2_D , χ^2_R , and χ^2_{DR} for a phased array located at $x_{rx,ph} = 250$ m and the refractive index model $n_{2010,6}^{CFM}(z)$. The best fit value is indicated with a red circle, whereas the true TX position used to initialize the MEEP simulation is indicated with a black cross.



(b) Reconstructed TX positions for phased arrays located at ranges $150 \text{ m} \leq x_{rx,ph} \leq 550 \text{ m}$. The points correspond to the mean value of $(x_{tx,reco}, z_{tx,reco})$ among the ice models, while the error-bars show the standard deviation of the range and depth among the ice models.

FIG. 23: Left (23b): penalty score map over TX range. Right (23b): reconstructed TX positions.